Near-field Probing Array for Enhancing 5G mm-wave Beamforming Transmitter Performance

by

Yushi Cao

A thesis
presented to the University of Waterloo
in fulfillment of the
thesis requirement for the degree of
Master of Applied Science
in
Electrical and Computer Engineering

Waterloo, Ontario, Canada, 2021

Author's Declaration

I hereby declare that I am the sole author of this thesis. This is a true copy of the thesis, including any required final revisions, as accepted by my examiners.

I understand that my thesis may be made electronically available to the public.

Abstract

As sub-6 GHz fifth-generation (5G) communication networks begin to deploy commercially, the industry is seeing a paradigm shift towards the millimeter wave (mm-wave) bands as they provide multi-gigahertz of frequency spectrum and the potential of multi-gigabit data rates with ultra low latency. Intensive research efforts have been put into realizing competitive mm-wave hardware to support the increasing demand for high speed connections and data throughput. This hardware relies on modern semiconductor technologies that still face the challenges of low gain and output power at such high frequencies. When compounded with the high path loss at mm-wave, and the needs of multi-input multi-output operation, the transceivers must be implemented as beamforming phased arrays.

Although beamforming phased arrays offer many advantages, there are short-comings associated with them that need to be addressed. In the current landscape, a beamforming array with self-calibration capability, linear power amplifier (PA) response, and low production cost is highly desirable. This thesis is written amid these challenges. This work designed and fabricated an antenna-on-PCB (printed circuit board) RF beamforming array at 28GHz with 4 GHz operation bandwidth and $\pm 50^{\circ}$ steering range. The array incorporates a novel embedded near-field probing array for the purpose of providing feedback signals for self-calibration and PA linearization using digital pre-distortion (DPD). Using the proposed near-field based calibration procedure, the array output's amplitude and phase root-mean square variations between elements are 0.27 dB and 2.8°, respectively. Using the near-field based DPD, the adjacent channel power ratio and error vector magnitude improved from 30 dB and 8.8% to 39 dB and 2.5%, respectively, for a 400MHz OFDM signal.

Acknowledgements

I would most importantly like to thank my parents, Xinge and Jinmei, my aunt Xinyong, for supporting my Canadian study journey, without whom this thesis would not have been possible.

I would like to thank Professor Slim Boumaiza for his guidance and support in my final year of undergraduate and the two years of graduate study, for his excellent mentorship, and for providing resources for my research, and career and life growth.

I would like to thank Ahmed Ben Ayed and Jingjing Xia for helping me extensively, from theory to design and lab measurement, and for their endless patience in answering my questions.

I would like to thank my girlfriend Huixin Jin, my dearest friend, for not only the companionship but also the academic discussions whenever I need.

Last and certainly not least, I would like to thank all EmRG colleagues who have participated in conversations with me and provided logistics. In specific, Giovanni Scarlato and Ifrah Jaffri.

Table of Contents

List of Figures

List of Tables

Chapter 1

Introduction

1.1 Motivation

As rapid advancements in technology have occurred in recent years, wireless connectivity has played a core role in facilitating the ever increased demands for mobile data, internet of things, artificial intelligence, remote medical services, smart cities, and any technology that requires or relies on a mobile data connection [25]. These areas of application have stimulated exponential growth in mobile data traffic [8]. As the demand climbs, mobile technologies are also advancing. Intense research efforts have been put into the 5th generation (5G) mobile network. Compared to older-generation mobile networks, 5G is meant to deliver higher data speeds (in the magnitude of multi-gigabits), lower latency (down to milliseconds), and more network compatibility [29].

Mobile carriers began to launch sub-6 GHz 5G services commercially within the last few years, achieving higher data speeds and lower latencies compared to older technologies. However, they are not able to meet the stringent multi-gigabit and millisecond throughput and latency requirements. This is because the sub-6 GHz frequency bands have limited bandwidth to use and the spectrum is crowded with existing technologies such as 3G and LTE (Fig. 1.2). Millimeter-wave (mm-wave) 5G will offer a solution; at mm-wave frequencies, there are gigahertz of available spectrum and the channel bandwidths can be hundreds of megahertz [2], enabling gigabit data speeds. However, there are inherent technical challenges associated with mm-wave radio, such as lower amplifier gain and power and higher propagation path losses. To counter these issues, more advanced technology nodes need to be used, and multiple transmitters (Tx) / receivers (Rx) are often needed to work together to achieve the desired power level. The shorter wavelength at mm-wave

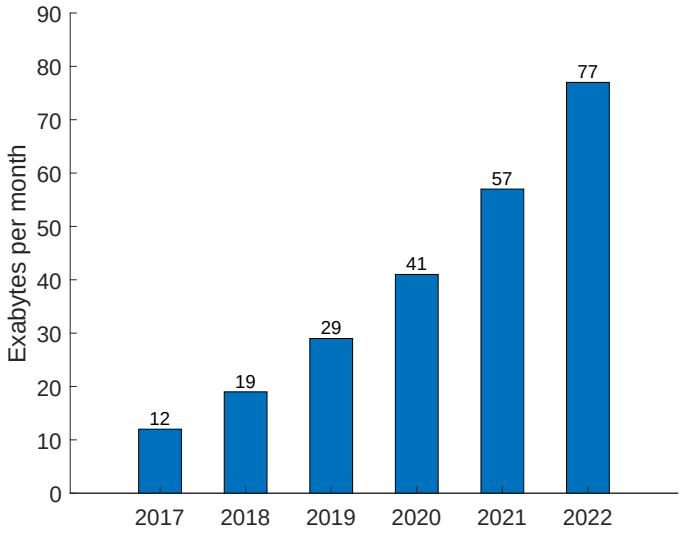

Figure 1.1: Average monthly global mobile data traffic [8]

frequencies also requires the circuit components to have very small footprints and usually demands high system integration. These stringent requirements force the system integrator to use advanced fabrication and assembly processes, which drives up the production cost. As a result, significant research efforts have been put into mm-wave technologies for a variety of applications.

1.2 Problem Statement

Given the low powers and high propagation losses experienced at mm-wave frequencies, a Tx or Rx usually has multiple elements with multiple antennas working simultaneously as an array. In a radio frequency (RF) beamforming array where all elements are expected to transmit or receive the same signal with only phase and magnitude being different, the signal's power and quality improvements rely on the consistency of each element. When the elements are set to operate at the same settings, each element should output the same amount of power, and their phase should be coherent. In reality, however, this is not the case as manufacturing process variations introduce amplitude and phase variation between elements. Thus the array must be calibrated before entering service, not to mention that during the life span of the equipment re-calibration is needed to control performance degradation due to ageing and changing environments. As a result, an array with in-field

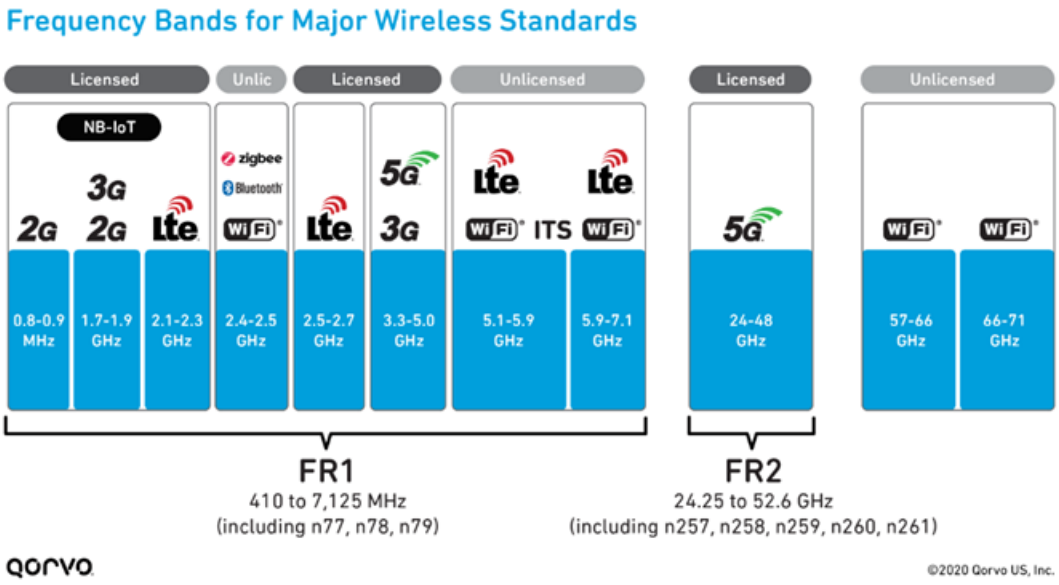

Figure 1.2: Frequency bands for major wireless standards [28]

calibration capability is desirable.

The power amplifier (PA) of the 5G mm-wave Tx is operated near the non-linear region to achieve optimal power and efficiency. However, the signal is modulated using high-order modulation schemes with high peak-to-average power ratios (PAPR). As a result, the signal's quality is significantly degraded due to non-linear distortion. Digital pre-distortion (DPD) can be introduced to linearize the PA; however, in order to operate the DPD properly, the array must have a feedback mechanism implemented. This is difficult to achieve due to the small component size. So, a realizable feedback implementation is critical to successful Tx operation.

In summary, this thesis addresses the problem of needing a mm-wave RF beamforming array that

1. enables reliable and cost-effective array calibration, and
2. incorporates a realizable feedback mechanism for DPD.

1.3 Thesis Organization

This thesis is organized as follows.

Chapter 2 presents background material on the relevant topics, the basic concepts of beamforming are summarized, and recent works in the literature are reviewed. The theory of near-field based RF beamforming array calibration techniques is described and formulated in Chapter 3. Chapter 4 contains a detailed description of the design and simulation of the proposed RF beamforming array and near-field probes; the chapter also briefly reviewing the design spaces available, comparing each option. Performance measurement results for the fabricated prototype array are presented in Chapter 5. Lastly, the thesis concludes with Chapter 6, in which conclusions are presented and recommendations are made for future work.

Chapter 2

Background and Literature Review

2.1 Background

2.1.1 Beamforming and Beamforming Arrays

The beamforming array is one of the key building blocks of a 5G mm-wave radio system. It is responsible for radiating and receiving radio waves for wireless communication so that its performance has a major impact on the overall link quality. The beamforming array consists of an array of RF beamforming transceivers and antennas, and typically one antenna is fed by one RF front-end, which is defined as one element. The array can technically have any shape, but for practicality and beamforming requirements, they are usually arranged in a line or on a two-dimensional (2D) plane which are referred to as linear array and 2D array, respectively. Different elements can radiate or receive different waves; since the waves can interfere with each other, i.e. they can combine constructively or destructively, illustrated in Fig 2.1, one or multiple beams can form over the medium. By setting each array element carefully, the number of beams and their directions can be controlled, which allows the signal to be transmitted towards or received from only desired directions. This is important for 5G mm-wave communication for a few reasons:

1. **Path loss**: According to Friis equation, the loss of electromagnetic (EM) waves traveling in free space is calculated in (2.1):

$$L(dB) = 20 \times log_{10}\frac{4\pi d}{\lambda} \tag{2.1}$$

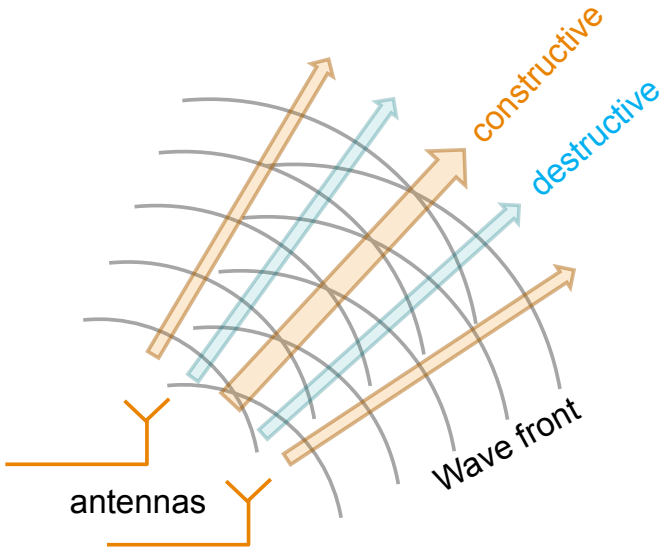

Figure 2.1: Wave interference from two sources (array elements)

where d is the distance between the Tx and the Rx, and λ is the wavelength of the EM wave. It is seen that, for the same link distance, the shorter the wavelength, the higher the propagation loss. At mm-wave frequency, the wavelength is smaller than $10mm$, which makes it unrealistic for broadcasting, and calls for directional radiation that concentrates the power in only one or few narrow beams.

2. **Spacial multiplexing**: By only radiating a certain direction, the Tx can simultaneously transmit at multiple Rx at the same frequency and time; it should be noted that the signals for each Rx do not need to be the same. This greatly increases the efficiency of the communication system, as the same frequency channel can be used for multiple users.

3. **Multi-input multi-output (MIMO)**: Because of the ability to shape the beams, one or more Tx can code their beams in a way such that they can serve multiple Rx at different locations with different data at the same time. This is achieved by coding the signals in the digital domain so that only the useful information is added constructively at each Rx, while unwanted data is cancelled.

By grouping the elements and connecting to the baseband circuitry in different ways, beamforming arrays can be classified into three types: RF (or analog), digital or hybrid.

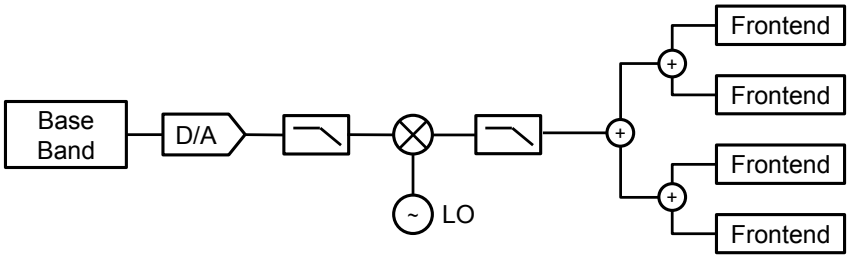

Figure 2.2: Simplified block diagram of an RF beamforming array

1. **RF beamforming array**: In an RF beamforming array, all elements are fed by the same digital baseband such that all elements are transmitting or receiving the same signal, with the only difference in the analog beamformer setting: amplitude and phase. A typical architecture of an RF beamforming array is illustrated in Fig 2.2: only one digital stream is used to feed the array, the analog signal, $x(t)$, after the digital-to-analog converter (DAC) and up conversion is equally splitted into N channels, then the same analog signal, $x'(t)$, is fed to all array elements. The analog beamformer consisting of amplitude and phase control circuitry adjusts the input signal, and outputs to the antenna. The beamforming is achieved by setting the amplitude and the phase of each element appropriately. For example, for a linear array operating in receiving mode, illustrated in Fig 2.3, the elements are equally spaced $0.5\lambda(180°)$ apart at their center frequency, the incoming plane wave arrives at angle θ from the normal of the array. In this case, element 1 receives the signal at phase α_1, for example, $x(t)e^{j\alpha_1}$, then element 2 would receive $x(t)e^{j(\alpha_1+\pi sin(\theta))}$, and element N receive $x(t)e^{j(\alpha_1+\pi sin(\theta)\times(N-1))}$. Therefore, for element $i \in [1, N]$ in the array, if its phase shifter is set to $-\pi sin(\theta) \times (i-1)$, then it would output:

$$\begin{aligned} y(t) &= x(t)e^{j(\alpha_1+\pi sin(\theta)\times(i-1))} \times e^{-j\pi(sin(\theta)\times(i-1))} \\ &= x(t)e^{j\alpha_1}. \end{aligned} \tag{2.2}$$

   Therefore, all elements output the same signal with the phase aligned. As this alignment only happens for waves coming at angle θ, a beam is formed at that angle. In transmit mode, the analysis is the same only now the array is transmitting a beam in θ direction.

   The theory can be extended into an irregular and 2D array with the addition of ϕ steering. Illustrated in Fig. 2.4, element (0,0) is used as a reference, for element (i,j) which is located (M, N) unit distance away from the reference, for beamforming at (ϕ, θ) direction its phase shift is calculated as

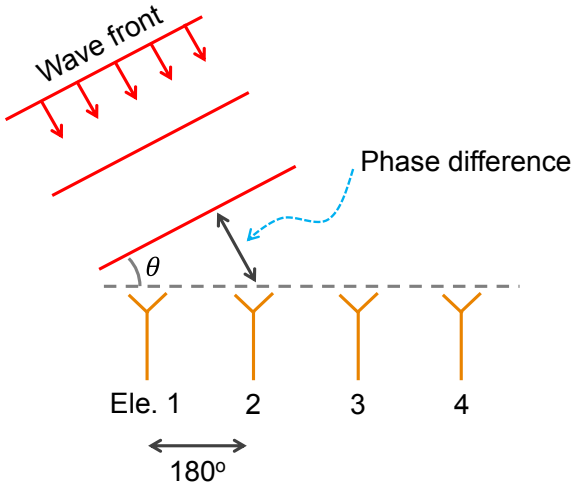

Figure 2.3: Beamforming example in a linear array

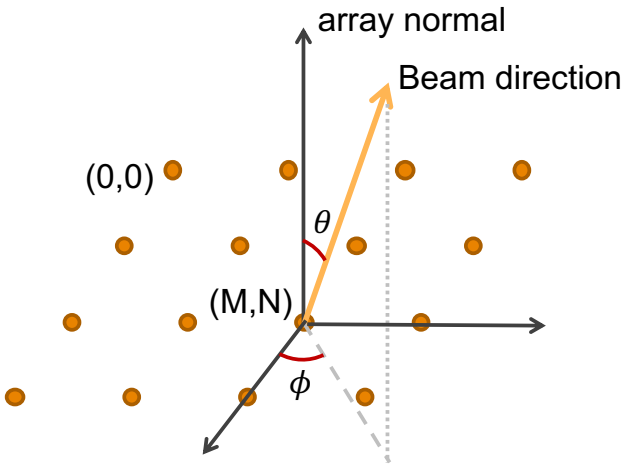

Figure 2.4: Beamforming example in a 2D array

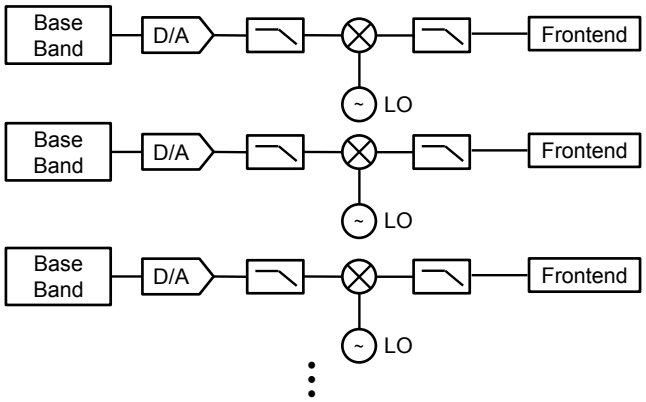

Figure 2.5: Simplified block diagram of digital beamforming array

$$p(M,N) = \frac{\sqrt{M^2+N^2}}{\lambda} \times cos(\phi - arctan(N/M)) \times 2\pi sin(\theta) \tag{2.3}$$

where λ is the free space wavelength at beamsteering center frequency.

Therefore the beam becomes steerable in a three-dimensional (3D) space. It should be noted that this equation is generic for 2D arrays with any element positioning since it takes its relative coordinate as the parameter.

2. **Digital beamforming array**: Different from an RF beamforming array, each element in a digital beamforming array has its own digital baseband, there are no analog beamformers in the chain, and the beamforming is achieved by manipulating the digital streams. A simplified block diagram is displayed in Fig. 2.5. Compared to RF beamforming, digital beamforming offers much greater flexibilities as the processing is performed in the digital domain, and digital coding can be applied to enable MIMO [40]. However, this flexibility comes at a great cost of hardware equipment and power consumption as each element runs its own baseband processor, DAC/analog-to-digital converter (ADC), and up- and down-converter. The numerous hardware also requires larger real-estate which is scarce at mm-wave frequency.

3. **Hybrid beamforming array**: A hybrid beamforming array is a conglomeration of RF and digital beamforming arrays. Illustrated in Fig 2.6, a hybrid beamforming array is constructed with multiple RF beamforming arrays, each with its own baseband. This configuration is a balance between the other two; it can be operated as a

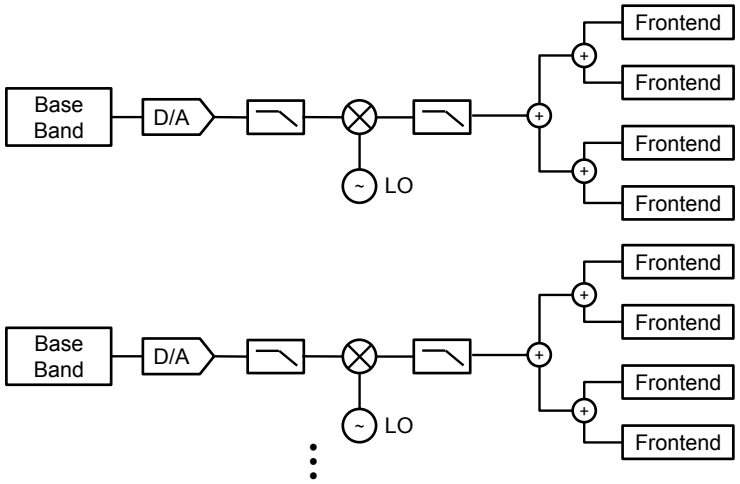

Figure 2.6: Simplified block diagram of hybrid beamforming array

digital beamforming array and digital coding can be applied to enable MIMO [36], or it can be operated as an RF beamforming array, given the sub-array spacing follows the same rule as in RF beamforming array. Because of the usage of digital precoding, the subarrays do not need to be placed at the same location, thus a mash of hybrid beamforming network in a 3D space is possible.

In recent research works, RF beamforming array was heavily investigated due to its relative ease of implementation, and ability to expand to hybrid beamforming array [37, 17, 22, 14, 41, 31, 32, 43, 15, 26, 16, 39, 18, 6, 7, 11]. This thesis focuses on designing and implementing an RF beamforming array with enhanced Tx performance.

2.2 Literature Review

Extensive research has been done on implementing mm-wave beamforming arrays for 5G communication, including all three architectures discussed previously. Although this thesis focuses on the RF beamforming array, the other architectures share similar or some common features and techniques, especially for hybrid beamforming arrays. This section of the thesis first reviews the existing state-of-the-art beamforming array implementation in literature, then reviews existing planar array near-field based calibration techniques and implementation.

2.2.1 Recent Ka Band Beamforming Array Implementation

The current 5G frequency range 2 (FR2) bands defined by The 3rd Generation Partnership Project (3GPP) are n257 - n261, which correspond to 24.25 GHz to 29.5 GHz and 37 GHz to 43.5 GHz [1], these roughly match the Ka band (26.5 GHz to 40 GHz). As a result, beamforming arrays targeted for Ka band have developed rapidly in recent years because of the release of the 5G FR2 standards and the gradual commercialization of mm-wave 5G.

There are two popular 2D array layout approaches: brick and planar. In a brick array, the array is implemented as a linear array first, typically on a printed circuit board (PCB), then multiple PCBs are stacked together to form the 2D array. Chun-Nien Chen demonstrated an array using this arrangement operating at 38 GHz targeted for 5G links [6]. Fig. 2.7 shows the build of this array: first, an 8-element PCB beamforming module is designed and built, which consists of PA, low noise amplifier (LNA), an 8-channel beamformer, as well as up/down converter. The module takes an intermediate frequency (IF) signal and local oscillator (LO) both at less than 5 GHz, the up/down converter has a built-in frequency multiplier which brings the LO up to RF frequency. Once the linear array is operating, multiple of them are assembled vertically to form a 2D array. The example in the figure shows a 4-PCB stack, with 32 elements in total; the IF and LO signals are the same for all 4 PCB modules. It should be noted that both the linear array and the 2D array maintain optimal element spacing for RF beamforming. Another point worth noting is that each module takes in IF and LO signals at IF frequency and they are only upconverted immediately before feeding into the beamformer. Although this requires separate up and down converters on each PCB module, the routing loss on and off PCBs is greatly reduced. The array achieves 50.1 dBm of effective isotropic radiated power (EIRP) at 38 GHz with $\pm 53^\circ$ steering range along the 8-element axis.

Toshihide Kuwabara and other authors in [16] also implemented a brick array at 28 GHz, shown in Fig. 2.8. The architecture is similar to that in [6], where multiple PCB modules are stacked together to form the 2D array. Different from the integrated solution in [6], this array uses GaN technology to implement the PA that delivers very high power (33 dBm saturated power), but it suffers from substantial thermal limitations. To help with the cooling, a heat pipe is used to conduct heat from the PCB to the back of the 2D array where fans are used to cool down the heatsinks. Because of the bulky heat pipes, the 2D array is not able to maintain optimal element spacing, as a result, the beamforming capability is limited, and the array is used for back-haul data communication. Overall, the array has an impressive 68 dBm EIRP with a 1700m coverage distance.

Another solution that uses a brick array is introduced in [7], similar to the others, the array consists of multiple stacked PCB modules, but here each PCB module also integrates

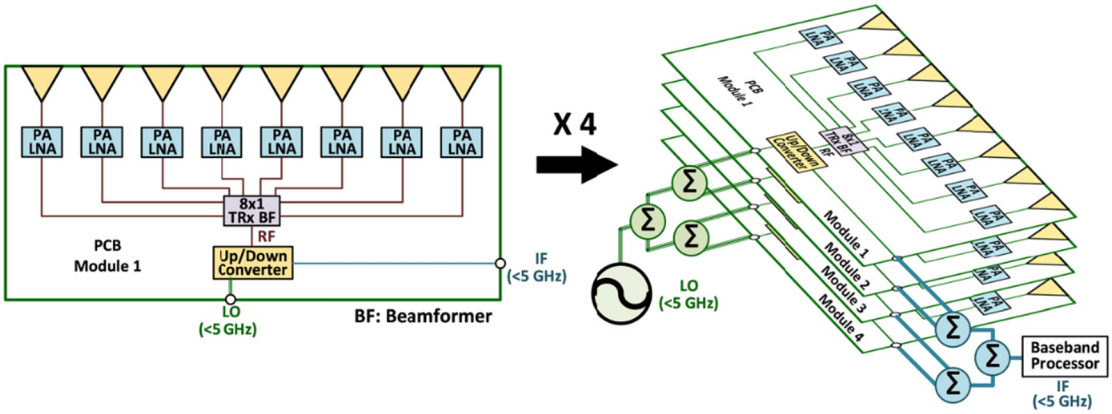

Figure 2.7: Brick array arrangement used in [6]

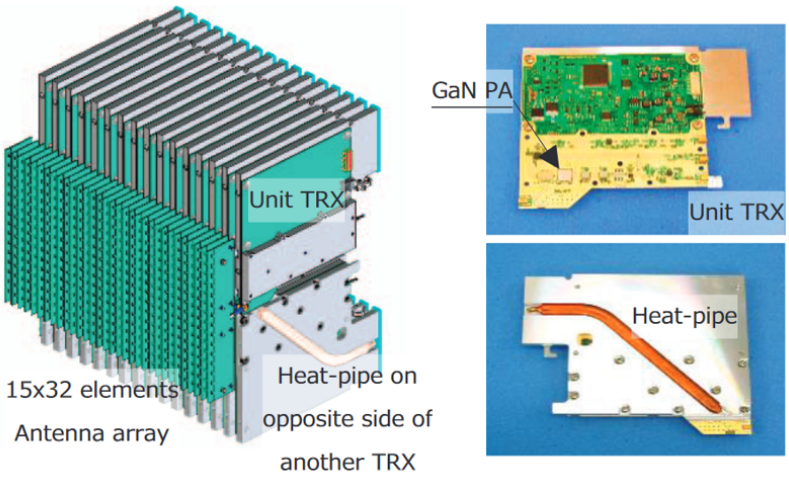

Figure 2.8: Brick array arrangement used in [16]

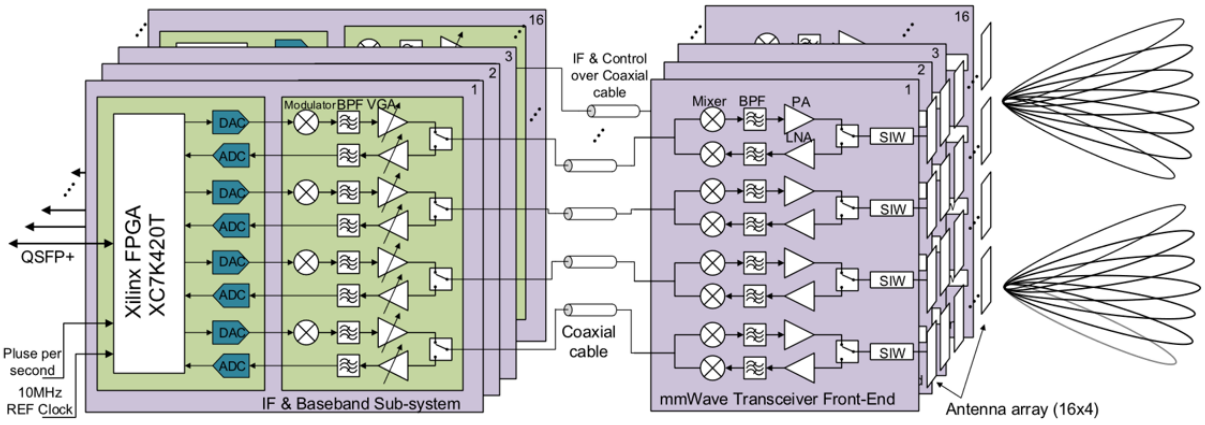

Figure 2.9: Digital beamforming array using brick configuration [40]

data converters. In this case, the 2D arrays can be operated as a hybrid beamforming array as each module is an RF beamforming array with separate digital data IO.

While most of the brick arrays are targeted for RF and hybrid beamforming, it is possible to make a digital beamforming array given the ample space on each PCB module. Binqi Yang from Southeast University demonstrated such a system in [40]. As the block diagram in Fig. 2.9 shows, a field programmable gate array with quad-channel data converters is used in each PCB module. The baseband signals are upconverted separately and are fed to separate antennas. Because of space and thermal consideration, all RF chains are developed in two sub-modules, one for baseband and up/down conversion, and the other for RF front-end and antenna. The RF signals from the two sub-modules are connected through cables, and the front-end and antennas are connected through bendable substrate integrated waveguides, illustrated in Fig. 2.10. By using digital beamforming and pre-coding, the beam coverage range achieves over $\pm 70^{\circ}$ with no grating lobe.

Because the brick arrays are stacked vertically, the antennas must radiate parallel to the PCB module, so, end-fire antennas must be used in this configuration. PCB based Yagi antennas are used in [6] and [40]; shown in Fig. 2.11a and b, the signal and reference branches are printed on the outer layers of the PCB, and fed through microstrip transmission lines. A PCB based Vivaldi antenna is used [7] (Fig. 2.11), the antenna is printed on the top PCB layer, and the feed is printed on the bottom layer.

Examining these works, the advantages of a brick array is summarized:

- Each PCB module is easy to design and implement: because of the low count of

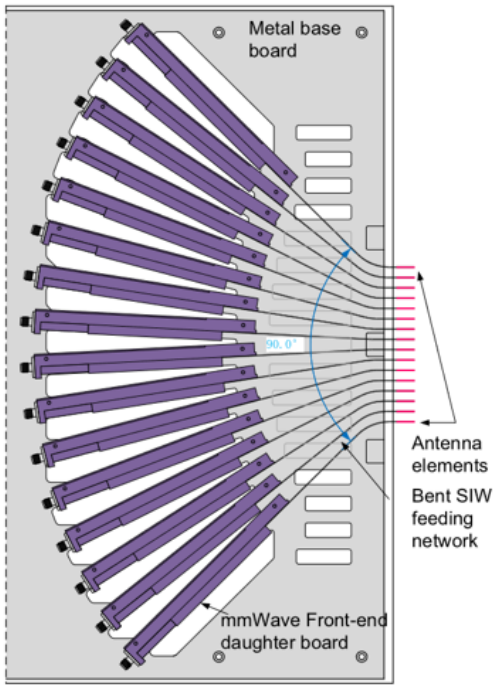

Figure 2.10: Front-end and antennas are connected through bendable substrate integrated waveguides [40]

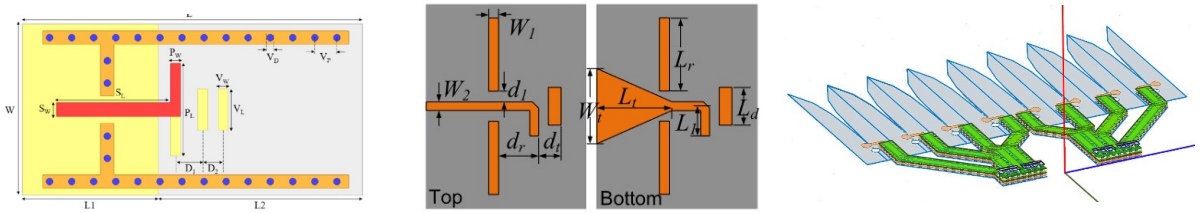

(a) (b) (c)

Figure 2.11: End-fire antennas presented in: (a) [6], (b) [40], (c) [7]

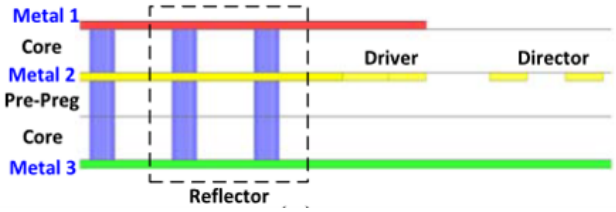

Figure 2.12: Brick array PCB stack up used in [6]

elements, and the linear array implementation, the floor planning is very easy, and space is typically not a constraint. The surface-mount devices and antennas can be implemented on the same PCB and on the same layers, so the PCB structure can be simple, which lowers production risks associated with PCB manufacturing. For example, the PCB used in [6] is from a regular 4-layer process which is considered simple in today's standard.

- Good modularity: After designing and manufacturing a PCB module (linear array), the array can be expanded into an unlimited large array by simply stacking multiple modules together. However, the width is still limited to the number of elements in the linear array.

- Possibly better integration: As presented in [7], because there is no limitation on the length of the PCB module, more components or RF building blocks can be integrated, such as up/down conversion, baseband processing, and power management unit.

At the same time, brick arrays have inherent disadvantages:

- Channel imbalance: because each array is formed by multiple modules, process variation may exist between them. They can be caused by PCB manufacturing, surface mount device misalignment, and also the assembly process of the 2D array. Since the beamforming performance depends on elements behaving uniformly, this variation can be a problem to the link signal quality.

- Thermal limitation: because the PCB modules are stack together closely, there is limited space between the boards to insert large heat sinks, so the 2D array must increase the board-to-board distance to facilitate sufficient cooling mechanisms, which breaks the antenna element optimal spacing.

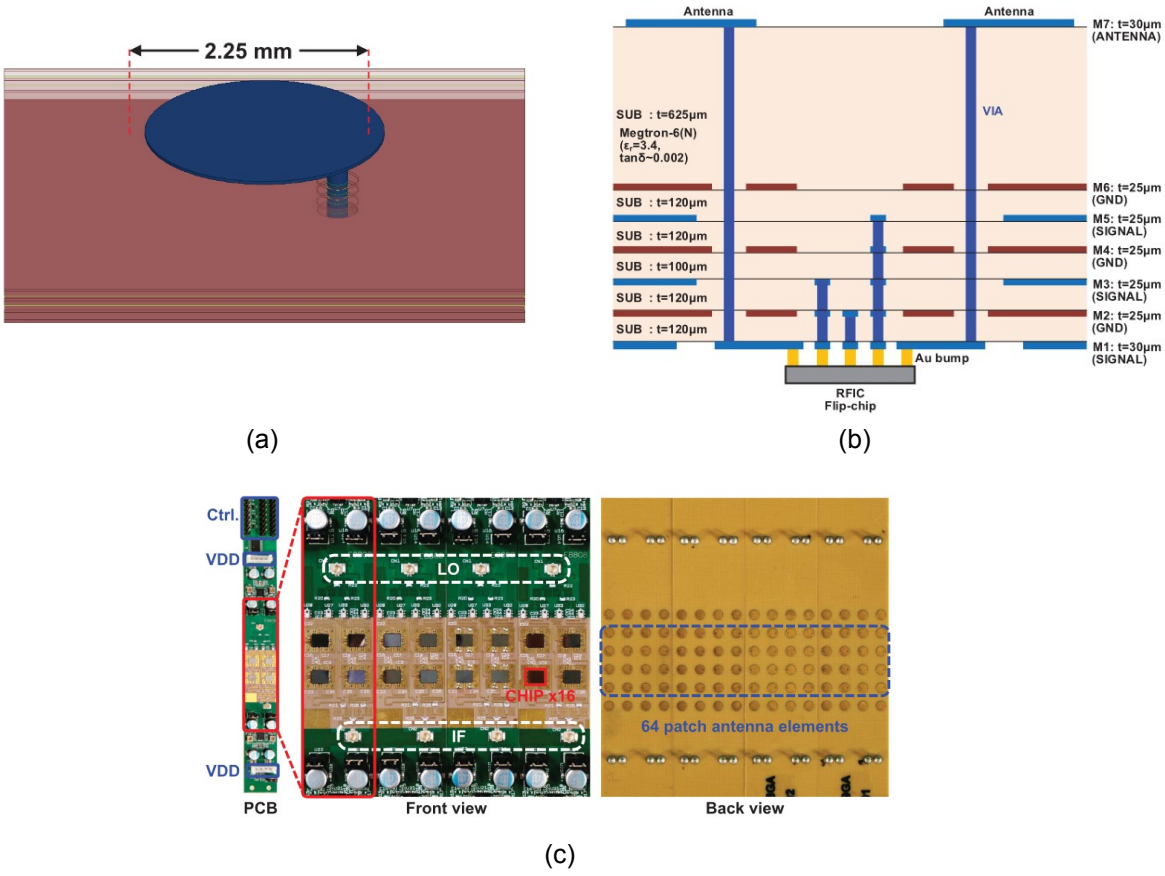

Figure 2.13: (a) Circular coaxial fed patch antenna design; (b) PCB stack up; (c) Top and bottom view of the array PCB

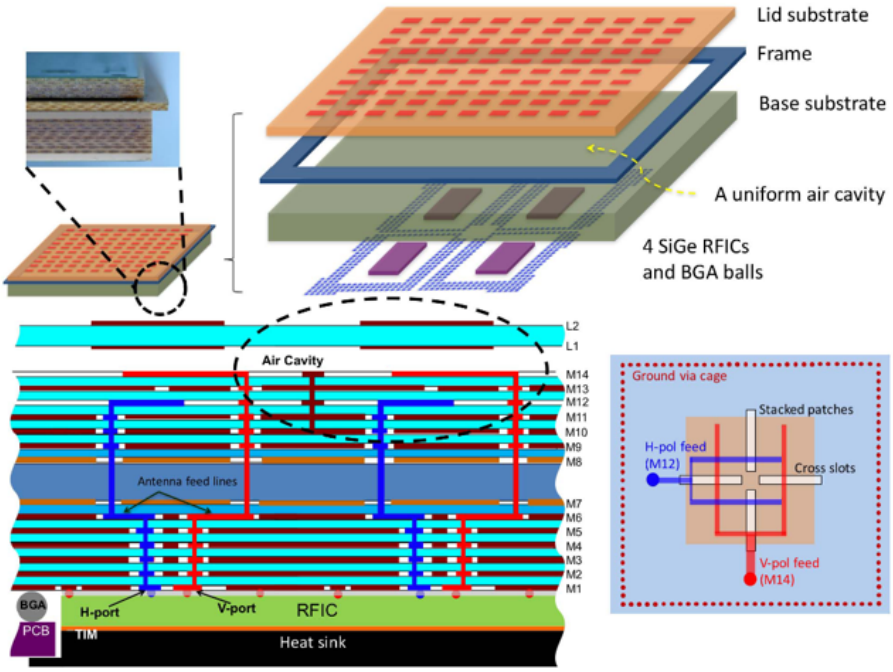

Figure 2.14: Assembly and stack up illustration for dual-polarized RF beamforming array [11].

For a planar array, the array is implemented directly in 2D, and the antennas must radiate perpendicular to the array plane. This configuration is much more prevalent than the brick array and is commonly seen in today's mm-wave array implementation. The antennas for this type of array are planar, for example, patches and dipoles implemented on PCBs are viable options. Yun Wang from the Tokyo Institute of Technology introduced a 39 GHz linear polarized 64-element RF beamforming array in [39] which uses circular patch antennas and targets a 5 GHz bandwidth. Displayed in Fig. 2.13, the system is integrated on a single PCB, where the quad-core beamforming RF integrated circuit (RFIC) is surface-mount attached to the bottom layer (M1) of the PCB, and the antenna is printed on the top layer (M7). The antennas are coaxial patches fed by through-hole vias. A few blind vias are built in the stack up to allow digital control signal and power routing of the RFIC. On the antenna layer, dummy antennas, which are terminated and not connected to the RFIC, are printed above and below the array. These are for improving the top and bottom row antenna performance [39].

One of the design features in this work is shown in Fig. 2.13c: each "blade" integrates

four RFICs and 16 antennas, and it is designed to have the width of four "element-spacing". As a result, multiple of these blades can be installed side-by-side to form a larger array. This approach reduces the risk associated with manufacturing a large array directly and adds more flexibility in terms of array size.

It is seen that the PCB stack up used in this work is significantly more complex than the ones used in brick arrays. This is because the stack up needs to support both the antenna design and the RFIC routing in a small area. In this example, quad-core beamforming RFICs are used with each connecting to 4 antennas (2×2). To ensure optimal element spacing, the routing of this RFIC must be confined within the 2×2 space and this requires multiple layers to realize. The planar antenna also requires more vertical space compared to an end-fire antenna, thus, the substrate between M6 and M7 are very thick.

For a dual-polarized design, the requirement on the PCB stack up becomes even more challenging. IBM demonstrated a dual-polarized RF beamforming array at 28 GHz, where the antennas are split into two sub-stacks [11]. Illustrated in Fig. 2.14, the patch antennas use proximity coupling and aperture feed, the feeds are printed on M12 and M14 layers, the patches are on L1 and L2 layers on a secondary PCB and there is an air cavity between the feed and the patches. The L1 layer patch is the main radiating patch and the L2 patch is a parasitic patch used to improve antenna bandwidth. This configuration greatly reduced the PCB manufacturing complexity because the main PCB (M1 to M14) can be implemented on a symmetrical high density internect (HDI) stack up while the antenna substrate thickness can be tuned by adjusting the air cavity height. The downside is that there could be variations in the assembly process and they will affect the result. The aperture is carved on M13 in a disconnected cross shape, shown in Fig. 2.14. This aperture layer also serves as isolation between the two feeds, which reduces the cross-polarization coupling. The antenna achieves 2 GHz bandwidth centered at 28 GHz and has around 7 dBi of gain for each polarization.

The beamforming RFIC is mounted on the bottom layer (M1), the antenna feed vias go through the stack through stacked microvias (M1 to M6, M9 to M14) and through vias (M6 to M9). By using an HDI stack up, the routing is flexible both in and across layers, for example, the feed vias show turns on M6 without via stubs. In this work, 16-core IC is used to feed 64 antenna elements, and there are 28 passive dummy elements surrounding the array.

However, it is still possible to implement a dual-polarized RF beamforming array without using the expensive HDI technology or excessive mechanical design. University of California San Diego presented an implementation in [22], where a regular 12-layer PCB is used and antennas are coaxial fed. Shown in Fig. 2.15 the patch antenna is also a stack

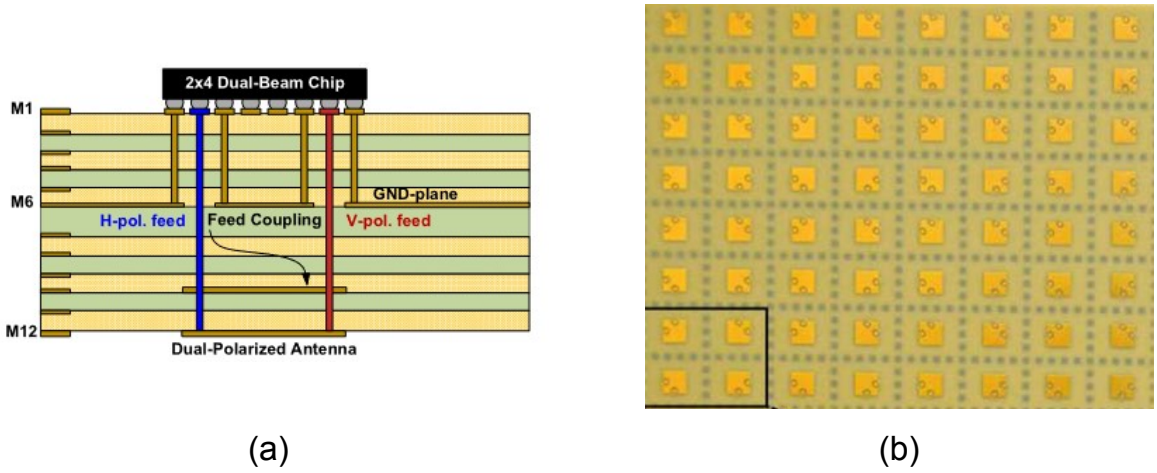

Figure 2.15: (a) Stack up illustration of dual-polarized RF beamforming array; (b) Rotating feed of dual-polarized array. [22]

patch design with the main patch on L10 and parasitic patch on L12. The antenna array design features rotating feeds so that the radiation generated from leaking magnetic currents in the cross-polarization cancels, thus improves the far-field cross-polarization rejection. In the measurement, this array achieves greater than 35 dB cross-polarization rejection at far field.

The authors in [17] implemented an RF beamforming array without using beamforming RFICs but with only distributed components for phase shifters, switches, PAs, and LNAs. This way, the array is not limited to CMOS technologies that are used in most beamforming RFICs, and high power technology such as GaN is used for PA. Using GaN PA, each channel achieves a stunning 39.5 dBm saturated output power at 28 GHz. Fig. 2.16 shows the implementation of the system: because all components are discrete, the radio front-end takes a large space, and the antenna cannot be integrated nicely. Therefore, the authors opted for a two-PCB design, the radio front-end, as well as drivers and up/down converters, are fabricated on one PCB, and the antenna arrays are implemented on another PCB. The two PCBs are connected by RF cables when operating. Nevertheless, the two-PCB approach still does not allow for optimal antenna element spacing for RF beamforming, so the array is aimed for high power backhaul communication, and the antenna unit cell spacing is chosen to be 1 λ.

In another work by San Diego, the antennas are directly integrated into the beamforming RFIC die, which is called wafer-scale phased array [15]. As Fig. 2.17 shows, the

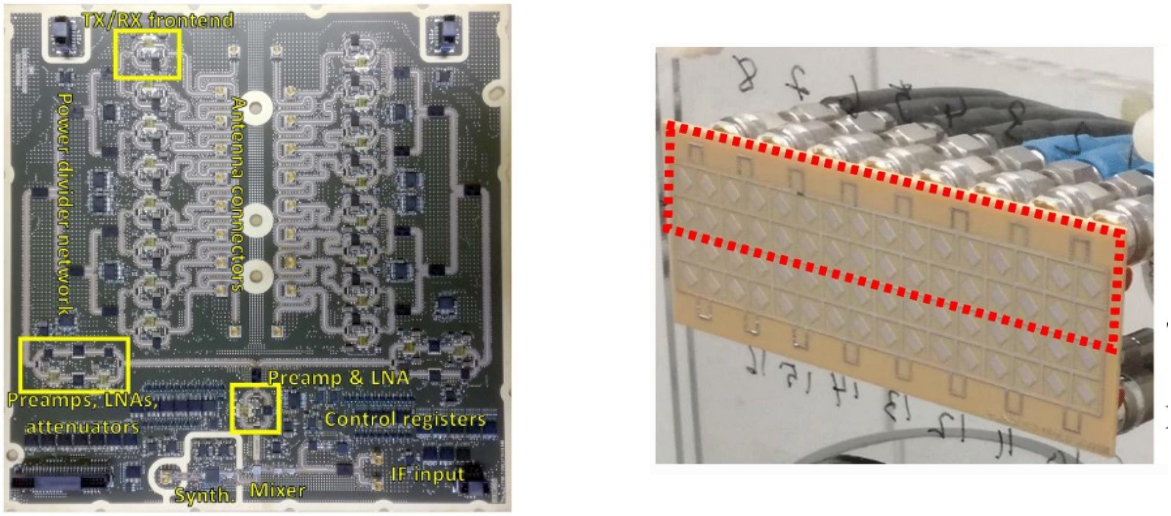

Figure 2.16: (a) Radio transceiver PCB of 28 GHz RF beamforming array; (b) Antenna PCB of the array

beamforming IC is implemented on silicon, and the stacked antenna is implemented on a quartz layer right on the top of the die. The feeding mechanism is proximity coupling and the feed is placed on the M7 layer of the die. Using this approach, the antenna achieves about 4 GHz bandwidth at 60 GHz (this work is higher than Ka band but it is worth covering). The PCB design is greatly simplified in this case because it only requires RFIC digital control and power routing.

Comparing to the brick arrays, the pros and cons of each architecture are summarized and listed in Table 2.1

2.2.2 RF Beamforming Arrays with Integrated Transmitter Observation Receiver

Because the beamforming array consists of multiple array elements, the balanced performance between elements is desirable, and any imbalance can degrade the array performance [35, 39, 37, 32]. Besides, because the PAs are operated in the non-linear region, digital pre-distortion (DPD) is commonly used for linearization [24, 5, 37, 42, 18]. For both calibration and DPD, a transmitter-observation-receiver (TOR) is needed to monitor the Tx's

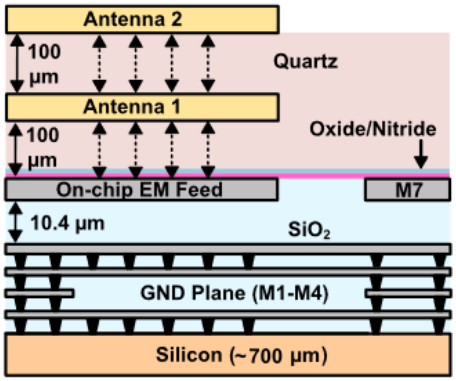

Figure 2.17: Stack up illustration of the wafer-scale phased array [15]

	Brick	**Planar**
Antenna type	End fire	Planar
Space required	Larger	Smaller
Modularity	Better	Worse
Flexibility	Better	Worse
PCB requirement	Simple	Complex
Mechanical design	Complex	Simple
Support for dual-pol	Hard, but possible to implement	Simple to implement

Table 2.1: Brick array vs. planar array

output; at mm-wave frequency, because of the implementation difficulty, an array with integrated TOR is highly desirable.

The most intuitive way of implementing such a mechanism is inserting couplers at the end of the Tx chain, usually after the PA. The authors in [17] and [37] demonstrated this design illustrated in Fig. 2.18. In this work, a long transmission line is routed near the output of all channels and couples to all of them. In operation, one channel is turned on at a time and the TOR receives the coupled signal from that channel. By comparing the de-embedded signals received by TOR from each channel, and adjust its gain and phase accordingly, the array is calibrated. Moreover, this mechanism can be used for collecting feedback signals needed for DPD engine training. However, there is one drawback in this design: although the coupler is implemented as a simple transmission line, it still takes extra space and forces the antenna spacing to be increased. In other words, this implementation limits the RF beamforming array's scanning range.

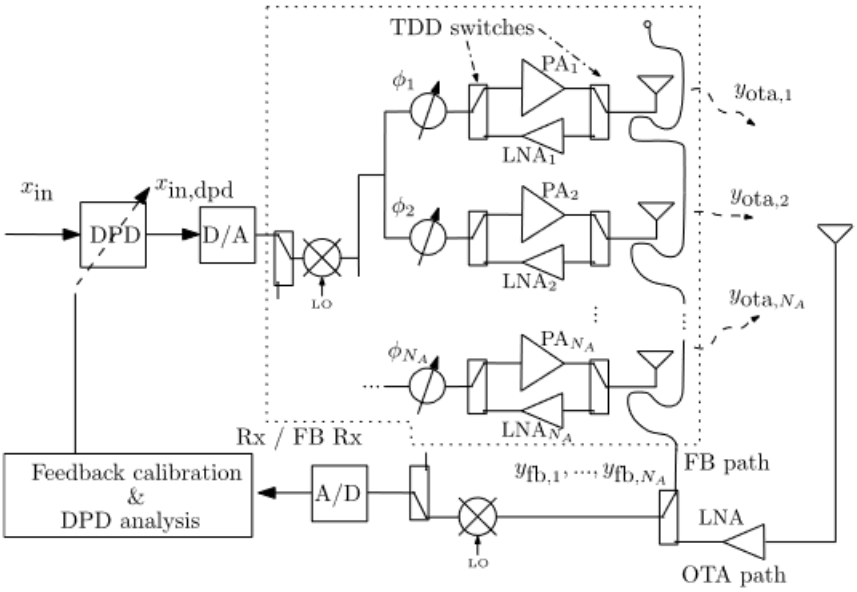

Figure 2.18: Transmission line (FB path) inserted after the TDD switch couples to all channels, thus "shared feedback" [37].

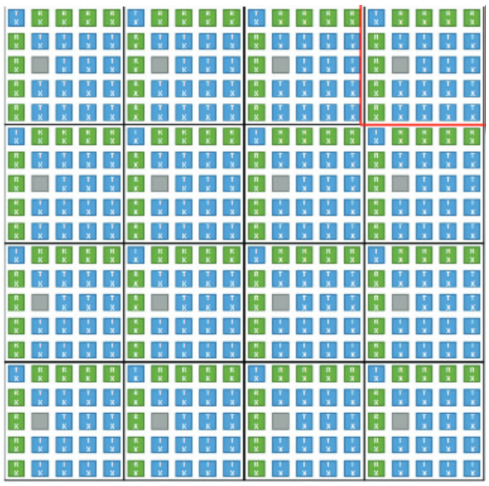

Figure 2.19: Antenna element layout in [20] – blue squares represent Tx, green squares represent Rx.

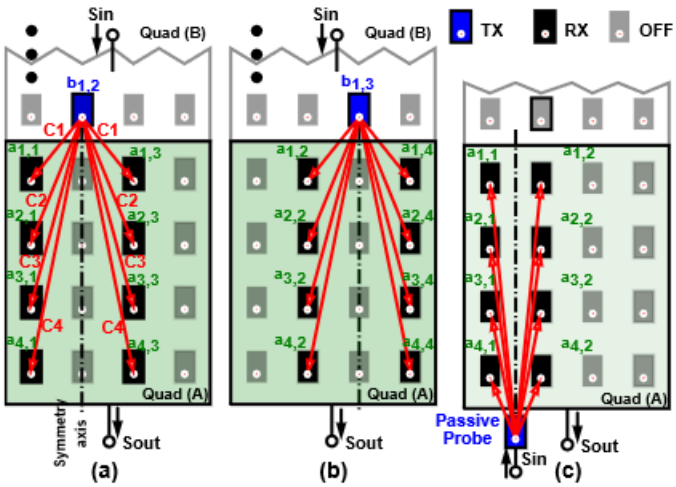

Figure 2.20: Calibration based on mutual coupling and symmetry of the array [21]

To avoid the space-consuming problem, it is better to reuse the existing components in the array. For example, [20] presented an array design where the Tx and Rx elements are separated and they have their own dedicated RF feeding lines, then they used the Rx chains as TOR based on antenna mutual coupling. The layout of the antenna array is displayed in Fig. 2.19. When the Tx elements are transmitting, the signal couples to the Rx elements and the received signal is used for training the DPD engine. As shown in the layout, the Tx elements roughly maintain optimal spacing in the W band, but the Rx elements are arranged in a net and their spacing is between 0.5 λ and 2.5 λ. Because of this, the steering capability in Rx mode is significantly reduced.

In [21], the authors proposed an innovative way to calibrate a hybrid beamforming array given the sub-arrays are placed side by side and the array size is not too large. The calibration is based on antenna mutual coupling and the symmetry of the array. As described in Fig. 2.20, because of the symmetry, the mutual coupling phase and magnitude between the calibrating elements (black) and the reference element (blue) are equal in each column. Therefore once the phase and amplitude relationship between the upper reference elements are found, the relative complex relationship between all columns is known. This is done by measuring the mutual coupling between the upper reference elements and the lower passive probe. After characterizing the column, the rows are characterized in a similar fashion, thus the relative phase and magnitude relationship between all elements are known, and can be used for calibration. Note that the upper reference elements are from the adjacent sub-array, and the lower passive probe is added outside.

This method is very elegant and, according to the measurement, effective. However, because it relies on the mutual coupling between adjacent sub-arrays the sub-array size is not scalable as a larger array will result in a very low mutual coupling level which leads to low signal-to-noise ratio (SNR) and poor calibration accuracy.

2.3 Discussion

Examining the phased array implementation and TOR integration, a few observations have been made:

- Planar antenna-on-PCB is the most common architecture for phased array operating at 28 and 39 GHz bands. Although a few brick arrays are demonstrated, the compact footprint and ease of mechanical design have made the planar array a more popular choice.
- Array's capability of in-field calibration is desirable. In order to maximize beamforming efficiency and quality, the array is calibrated to suit its operating condition including but not limited to device ages and external environments.
- Built-in feedback path for feeding TOR for DPD is an advantage. As an add-on to the array, the convenience this provides cannot be overlooked; because of the in-practicality of far-field based TOR, the embedded mechanism enables DPD training without additional setups. Although there are implementations with sacrificed element spacing or array size, a design without compromise is desirable.

In summary, one area of research is identified: beamforming phased array design with integrated TOR for DPD and array calibration. The innovation should be that the array element spacing is optimized for beamsteering, and that the TOR implementation does not depend on or limit the beamforming array size. At the time of writing this thesis, no other literature has shown a solution.

Chapter 3

Theory of Transmitter Performance Enhancement using Transmitter Observation Receivers

The transmitter is one of the key building blocks in an RF system, the transmitter performance will dictate the transmitted signal quality, and directly impact the communication link's usability and reliability. A typical architecture of a beamforming transceiver is illustrated in Fig 3.1, which has the ability to adjust its gain and phase through the variable gain amplifier (VGA) and the phase shifter (PS). The Tx signal is then fed into the PA and finally radiated by the antenna into the channel. There are various implementations on the exact architecture, for example, [9] uses a vector modulator (VM) combined with a Doherty PA to enable power amplification, gain adjustment, and phase shift. After all, the important aspect of a beamforming transmitter is the ability to perform complex adjustments (magnitude and phase) to the output signal, in order to fulfil the requirement

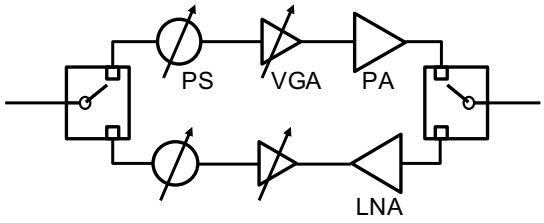

Figure 3.1: Typical beamforming transceiver architecture

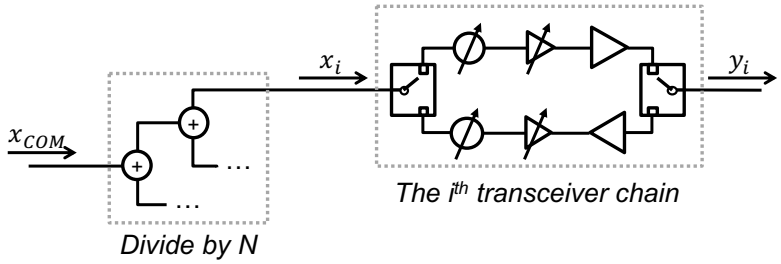

Figure 3.2: RF beamforming array transmitter calibration

of beamforming as discussed in the previous chapter.

In an array setup, there are multiple transmitters, sometimes over a thousand, and it is unreasonable to expect every transmitter, which houses several sub-building blocks, to have the same response. This is because of the manufacturing tolerance and process variation which can cause the internal difference in the performance of each individual transmitter. This difference is displayed as variation in input, output matching, gain, phase, etc. In a complete system, this variation can be amplified by external factors as well, for example, the uneven PCB trace width due to PCB fabrication tolerance, and uneven temperature profile for each transmitter due to non-ideal system placement or cooling mechanism. From the receiver's point of view, this transmitter variation results in degraded signal quality and beamforming capability [21]. Thus, transmitter calibration is often carried out after the array is built and/or deployed to ensure the best array performance.

3.1 Array Calibration Overview

For an RF beamforming array, there is one input to the array (RF common), as shown in Fig 3.2, label as x_{COM}. The RF common signal is equally split N ways to feed N transmitters, typically through an isolated divider, such as a Wilkinson power divider. The input to the i^{th} transmitter x_i, in a N-element array, is expressed the product of x_{COM}, and a imbalance factor m_i. Note that the division factor is absorbed into m_i. The transmitter applies magnitude and phase adjustment to its input, then the PA outputs the signal. This is expressed as y_i

$$y_i(\phi) = x_{COM} m_i w_i(\phi) e^{j\phi}, \tag{3.1}$$

where w_i is the complex-valued beamforming weight associated with beamforming phase setting ϕ. This value is the product of 3 terms: the combined VGA and PA gain, the phase-

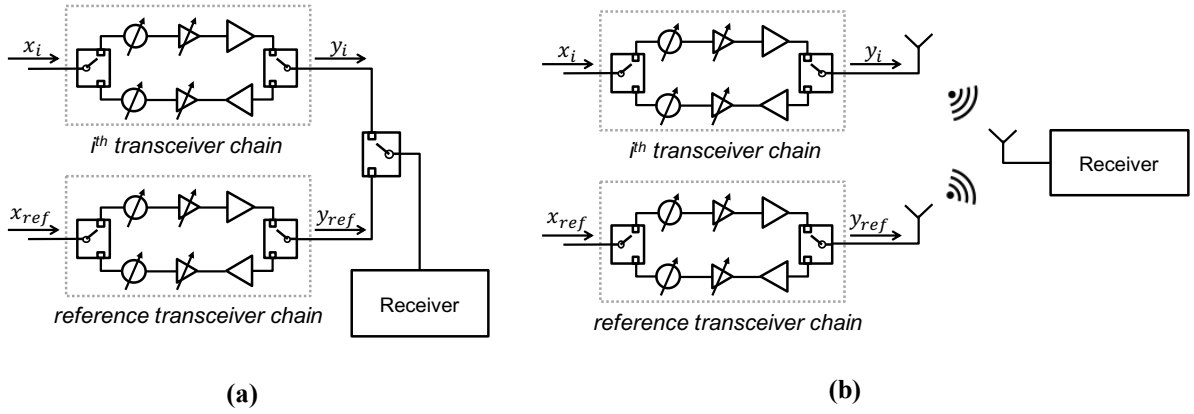

Figure 3.3: RF beamforming array transmitter calibration: a) conducted, b) far-field OTA based

shifting registered by the PS, and the complex error from the components' non-ideality. It should be noted that the error component of w_i is dependent on the beamforming phase setting ϕ due to the non-ideality of the PS. Now m_i and w_i can be combined into one complex term

$$\alpha_i(\phi) = m_i \times w_i(\phi), \tag{3.2}$$

and consequently,

$$y_i(\phi) = x_{COM}\alpha_i(\phi)e^{j\phi}. \tag{3.3}$$

In order for the receiver to receive a coherent combining of the waves coming from each transmitter, $y_i(\phi)$ needs to be the same for $i = 1, 2, ...N$, for every beamforming phase setting. Thus, all elements need to be calibrated individually across all ϕ to ensure $\alpha_i(\phi)$ have the same complex value in order to satisfy this requirement.

In a conducted testing environment, an array can be calibrated by conductively measuring the output of each transmitter chain ($y_i(\phi)$) and tune its VGA and PS, shown in Fig 3.3a. In this case, the conducted measurement path serves as the transmitter observation path for calibration. The array elements are turned on one by one, and $y(\phi)$ of each element is recorded. With all recorded data, a reference element (denoted by subscript $_{ref}$) is selected. Then the calibration coefficients γ are calculated as follows

$$\gamma_i(\phi) = \frac{y_{ref}(\phi)}{y_i(\phi)}. \tag{3.4}$$

Element i can then be calibrated by applying $|\gamma_i(\phi)|$ to its VGA gain setting, and $\angle(\gamma_i(\phi))$

to its PS. This process is performed for all ϕ values, therefore a lookup table can be constructed.

However, when the calibrated array is connected to antennas, the array may become un-calibrated again, this is because the load of each transmitter chain, i.e. the antennas' input impedance, are different from each other due to their different positions within the array that renders different boundary conditions and mutual coupling. In this case, when the transmitting array is placed in a channel, the receiver no longer sees uniform y_i, but rather $y_i \times s_i$ where s_i represents the complex transformation from the transmitter chain output to the far-field radiation. To avoid this problem, the beamforming array needs to be calibrated from the receiver point of view, thus a far-field transmitter observation receiver (TOR) is required, as illustrated in Fig 3.3b. In a real-world scenario, setting up a far-field TOR is unpractical and time-consuming, in addition, the calibration needs to be done regularly due to device ageing, and changing operating environments. Thus, there is a necessity for a feasible TOR to enable this calibration, and ideally, it should be applicable to arrays with any size

3.2 Digital Pre-Distortion Overview

Another application that relies on TOR is DPD. DPD is a technique used to linearize a non-linear circuit by pre-distort the input linear signal in the digital domain, such that the combined effects of the pre-distortion and the device distortion result in a linear signal. A typical application of DPD is to linearize non-linear PAs. A DPD engine samples the non-linear output signal to determine what pre-distortion to apply to the digital signal. There are many possible DPD algorithms, but all of them require TORs. Similar to the calibration discussed in the previous subsection, the TOR can be implemented at the transmitter output, for example, inserting a coupler [37], or it can be implemented as a far-field probe based TOR [24]. Although for the same reason as discussed before, the far-field based TOR is not always accessible.

3.3 Near-Field Based TORs

Because of the impracticality of far-field based TOR near-field based TOR attracted attention recently as a potential alternative. Instead of requiring setting up a far-field receiver, near-field TOR can be placed within the same setup as the transmitter, or even in the same package. [5] and [26] demonstrated the possibility of training DPD using near-field

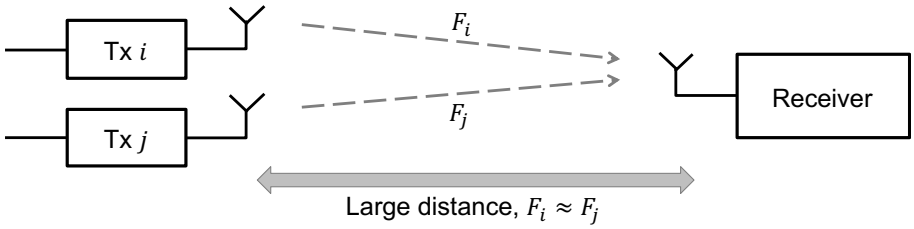

(a)

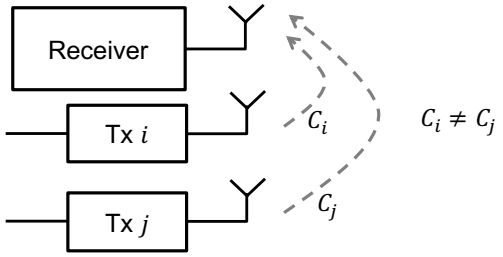

(b)

Figure 3.4: Beamforming array channels: a) far-field, b) near-field

probes to feed the TOR, where the probes are placed at the perimeter of the transmitting array, and they receive the transmitted signal through coupling. [21] introduced a similar approach by exploiting mutual coupling between subarrays in a hybrid beamforming array. Furthermore, authors of [20] use the receiving elements that are distributed inside the transmitting array to serve as TOR, also taking advantage of near-field coupling.

There is a major difference in theory of operation between a far-field based and near-field based TOR. At transmitting array far field, the channel between each radiating element and the far-field receiver is approximately equal, as shown in Fig 3.4a . Let the channel be F, then the far-field received signal from the i^{th} transmitter, y_i^{FF} is expressed as

$$y_i^{FF} = F \times y_i, \tag{3.5}$$

where y_i is the output of transmitter antenna i. It can be concluded that the calibration

process laid out in (3.3) - (3.4) is applicable in this scenario:

$$\gamma_i(\phi) = \frac{y_{ref}^{FF}(\phi)}{y_i^{FF}(\phi)} = \frac{y_{ref}(\phi)}{y_i(\phi)} \tag{3.6}$$

However, in the near field of the transmitting array, the channels between each radiating element and the near-field receiver are different, as illustrated in Fig 3.4b. In this case, the near-field received signal from the i^{th} transmitter, y_i^{NF}, is expressed as

$$y_i^{NF} = C_i \times y_i, \tag{3.7}$$

where C_i is the near-field channel between transmitting antenna i and the near-field receiving antenna. So the same calibration process would only be valid if C_i is know for $i = 1, 2, ...N$. Then the calibration coefficient γ can be calculated as following:

$$\gamma_i(\phi) = \frac{y_{ref}^{NF}(\phi)}{y_i^{NF}(\phi)} = \frac{C_{ref}}{C_i} \times \frac{y_{ref}(\phi)}{y_i(\phi)}. \tag{3.8}$$

These near-field channels can be acquired from EM simulation, or from a one-time far-field calibration following the steps:

1. Calibrate the array using the procedure described in out in (3.3) - (3.6)
2. After the array is calibrated at far-field, C_i is recorded for $i = 1, 2, ...N$ at any of the ϕ angles.

Note that there is a distinct difference between always calibrating the array in far-field and this one-time far-field calibration: the near-field channels are relatively constant in different environments, so the near-field channel only needs to be characterized once in a controlled environment, and any future calibration can be done using these constant C_i following (3.8), thus enabling in-field calibration.

The calibration coefficient γ is a function PS setting, so the calibration process (both far- and near-field) needs to be repeated for all ϕ angles.

With the near-field channel characterized, it is also possible to train the DPD engine using the near-field based TOR. By (3.7), the near-field TOR received any non-ideality from the transmitter (y_i), which forms the closed loop for DPD engine training. With near-field based TOR, the uses of couplers are eliminated, thus reducing overall form factor; far-field receivers are also not needed, enabling a compact self-contained package.

Chapter 4

28 GHz RF Beamforming Array Design with Embedded Near-Field Probing Array

From the literature review and theoretical discussion in previous chapters, it is clear that a beamforming array with embedded TOR is desirable for its ability to perform in-field calibration and DPD, both of which are essential for improving beamforming transmitter performance. However, there are also key design challenges that need to be addressed.

4.1 Project Scope

A 5G mm-wave beamforming array is typically integrated into a compact package, which is comprised of RFICs that integrates RF front-end, VGA, PS, as well as other necessary RF building blocks such as time division duplex (TDD) switches and power divider/combiner. Each RFIC typically supports 4 to 16 TRx chains, which can be connected to a 4-elements or 16-element linear polarized antenna array, or a 2-element, 8-element dual-polarized antenna array. Although RFIC with more TRx chains exist, they are usually for higher frequencies [12, 33]. The RFIC is mounted on a multi-layer PCB, which provides RF IO and digital IO to the IC. The PCB typically also integrates antennas, for example, planar patch antennas, and end-fire antennas [40].

In this project, the RFIC is an off-the-shelf product provided by Anokiwave (AWMF-0162), which is a quad-core (4 TRx chains) beamforming IC that operates from 26 to 30

GHz [3]. The project is designed around this chip, with the near-field probe in mind. A few key design blocks are:

1. Antenna-on-PCB and antenna array
2. Embedded near-field probing array within the RF beamforming array
3. RFIC footprint layout and its digital control logic
4. Other peripheral such as mechanical design

4.2 Antenna Design and Constraints

mm-wave antenna arrays for 5G communication are typically integrated with the RF front end on the same PCB or on two closely connected PCBs. This is to reduce the overall system size and to minimize potential RF performance degradation due to routing loss. However, the minimal size of the system poses challenges on PCB designs, because the manufacturability of the PCBs limits the design flexibility of the system, especially of the antennas. A few limitations and their impact on the antennas are discussed in this section.

4.2.1 PCB Building Process

The PCB is fabricated on one or multiple sheets of substrates (core), in the case of a multi-layer PCB, multiple sheets of core are pressed together with bond-ply material (prepreg). Because both core and substrate are pre-fabricated by the substrate manufacture, the PCB designer has to choose between a few pre-defined options. For example, the designer can choose to use a combination of cores and prepreg to achieve a certain substrate thickness, but it is unlikely that the thickness is the optimal value due to finite thickness resolution, so the designer needs to work around this constraint and optimize their circuits accordingly.

Another aspect of the stack up is via. A via is a vertical connection between different layers within a PCB, manufactured by drilling hole using mechanical drills or laser, and applying copper plating. The available vias for a PCB depend on the manufacturing process; the two common ones are multi-lamination and high density interconnect (HDI). In a multi-lamination PCB, the stack up is built from bottom to top; in each lamination cycle, a through via can be built, shown in Fig. 4.1. The vias drilled in the intermediate lamination cycles are covered by latter cycles, thus become blind vias. Note that if the

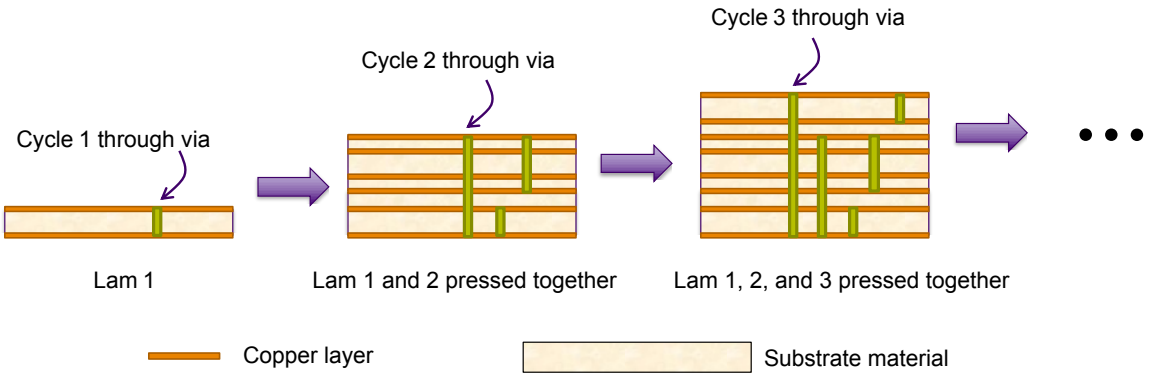

Figure 4.1: Illustration of multi-lamination PCB build process

laminations are the same for different cycles, they can be built at the same time to reduce production costs. This is illustrated in Fig. 4.1 where Lam 1 and Lam 3 uses the same build. The drawbacks of multi-lamination PCB for RF applications are:

1. laminations are built sequentially, so when applying them together, they need to be precisely aligned. The difficulty and cost are increased as the cycle increases. Thus it there is usually a limit on how many cycles a PCB manufacture can support.

2. because each blind via is built as a through hole, they need to be plated before the next lamination is applied. Therefore the common layer (bottom layer in Fig. 4.1) is plated multiple times and becomes very thick and unpredictable, which potentially harms the RF performance, and the designers must account for this thickness uncertainty.

In an HDI stack up, the PCB is built from the middle layer to the outer layers, shown in Fig. 4.2. Similar to multi-lamination, vias, typically laser drilled in this case, is manufactured in each lamination cycle. By using different combinations of vias, HDI provides more flexible via options where more buried vias can be manufactured starting and ending in almost all middle layers. Although HDI is more suitable for high density and high complexity systems, it requires a longer manufacturing time and cost because it is essentially double-sided multi-lamination. More importantly, because the HDI blind vias are not built in the same lamination cycles and they are stacked by multiple vias, the HDI blind vias will suffer from two drawbacks:

1. The multi-lamination cycles require the vias to have an annular ring on each layer,

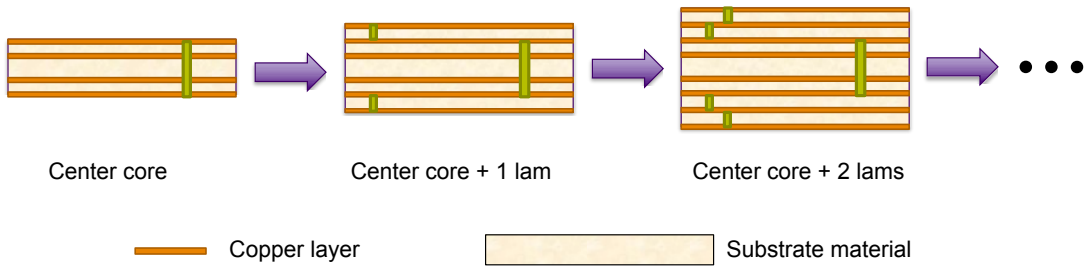

Figure 4.2: Illustration of HDI PCB build process

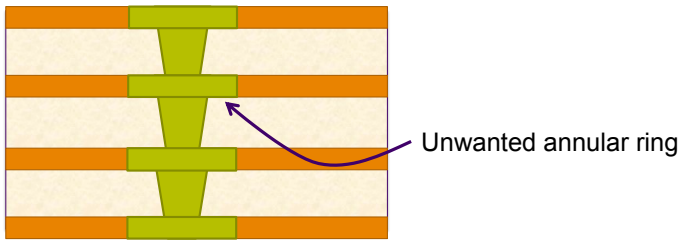

Figure 4.3: Illustration of HDI stacked via

thus the vias are not smooth, shown in Fig. 4.3. These annular rings add more parasitics to the system which are undesirable to RF applications.

2. The manufacturing tolerance between lamination cycles leads to misalignment, resulting in non-straight blind vias. This also degrades high-frequency performance and should be avoided.

Based on this comparison, a multi-lamination stack up is chosen for this project because of the superior blind via performance which is critical in ensuring an unbiased design and maximizing the beamforming array's potential.

4.2.2 Antenna Structures

In order to minimize the distance and loss between the antenna and the RF front end, the antenna is to be manufactured directly on the PCB. As discussed before, there are two popular antenna types for mm-wave 5G beamforming arrays: end-fire antenna and planar patch antenna.

An end-firing antenna, as its name suggests, radiates towards the end (or edge) of the PCB, shown in Fig. 4.4a. The antenna can be a dipole or Yagi-Uda, but the common arrangement for the beamforming array is shown in Fig. 4.4b. In this illustration, four-channel RF beamforming integrated circuits (ICs) are used, and the linear array can be expanded to a larger size by using multiple RF beamforming ICs and an RF distribution network. The linear array can then be extended to a 2D array by stacking multiple PCBs vertically, illustrated in Fig. 4.4c, enabling beamsteering in all directions. The advantage of the end-fire antenna array is that the PCB stack up is relatively simple because there are not as many vertical connections (vias) in the PCB. Another advantage is that the array can be easily expanded into a larger size by stacking more linear sub-arrays. However, because all RF connections are planar (as opposed to vertical), each PCB is relatively large. The more important challenge in implementing multiple stacked subarrays is the thermal constraint: because the optimal spacing between antennas is around 0.5λ [13], at mm-wave frequency, the spacing is very small so that the heat generated from the ICs on the middle PCBs is hard to get removed. [16] demonstrated an end-fire array with heat pipe cooling, but the spacing is increased to approximately 0.8λ, and the beamsteering range is significantly reduced.

A popular alternative antenna implementation for 5G mm-wave communication is planar patch antennas. Different from an end-fire antenna, a patch antenna radiates in the normal direction of the PCB. Fig. 4.5a shows an example of the cross-section of a patch antenna integrated with an RF beamforming IC: the IC is attached to the bottom side of the PCB, and the antenna is fabricated on the top layer. Because of this vertical configuration, a complex PCB stack up is required; however, this also results in a compact design, as the overall footprint of the antennas and the ICs is small, illustrated in Fig. 4.5b. This configuration does not require complex cooling systems, heat sinks can be directly attached to the back of the IC, and fans or other thermal peripherals can be installed without obstruction. However, the modularity of a patch antenna array is worse than that of an end-fire antenna array, although this thesis will demonstrate a modular design, it is not straightforward to expand a fabricated array to a larger size.

The RF beamforming array introduced in this thesis uses a planar structure, where patch antennas are selected for their easier design process and ability to incorporate near-field probes which will be discussed in later sections.

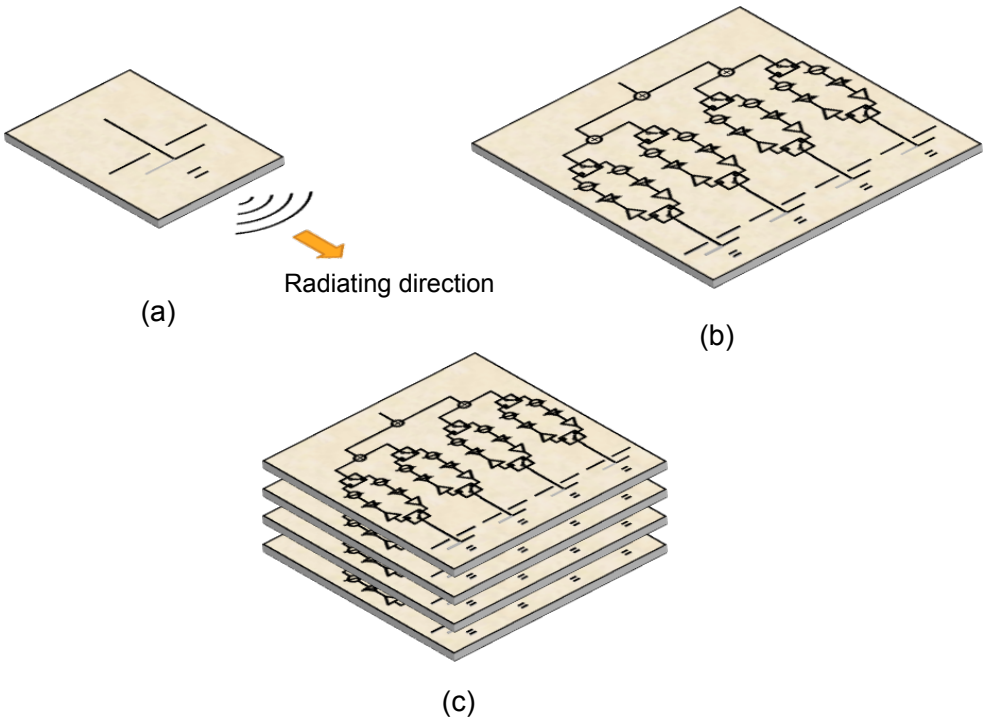

Figure 4.4: (a) Endfire antenna; (b) Typical 4-element beamforming array using endfire antennas; (c) Multiple stacks of 4-element arrays form 2D array

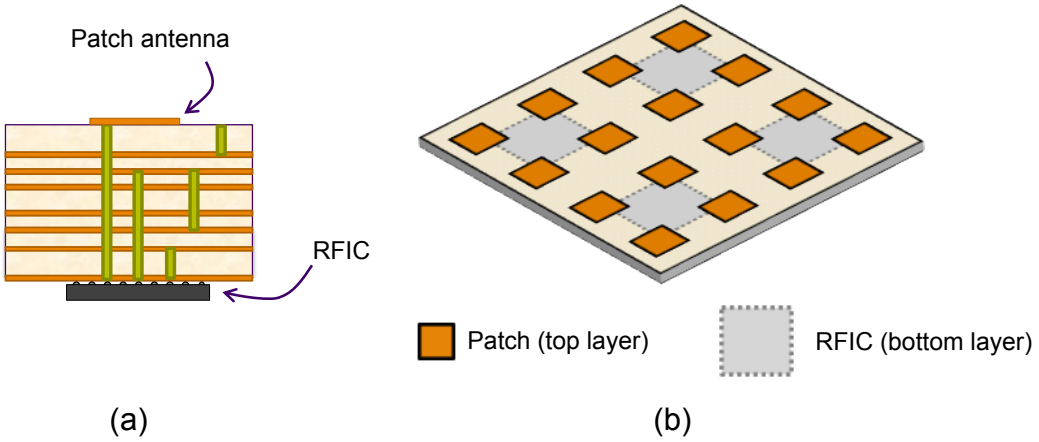

Figure 4.5: (a) Patch antenna on PCB integrated with beamforming RFIC; (b) Typical 16-element 2D patch antenna array integrated with four quad-core beamforming ICs

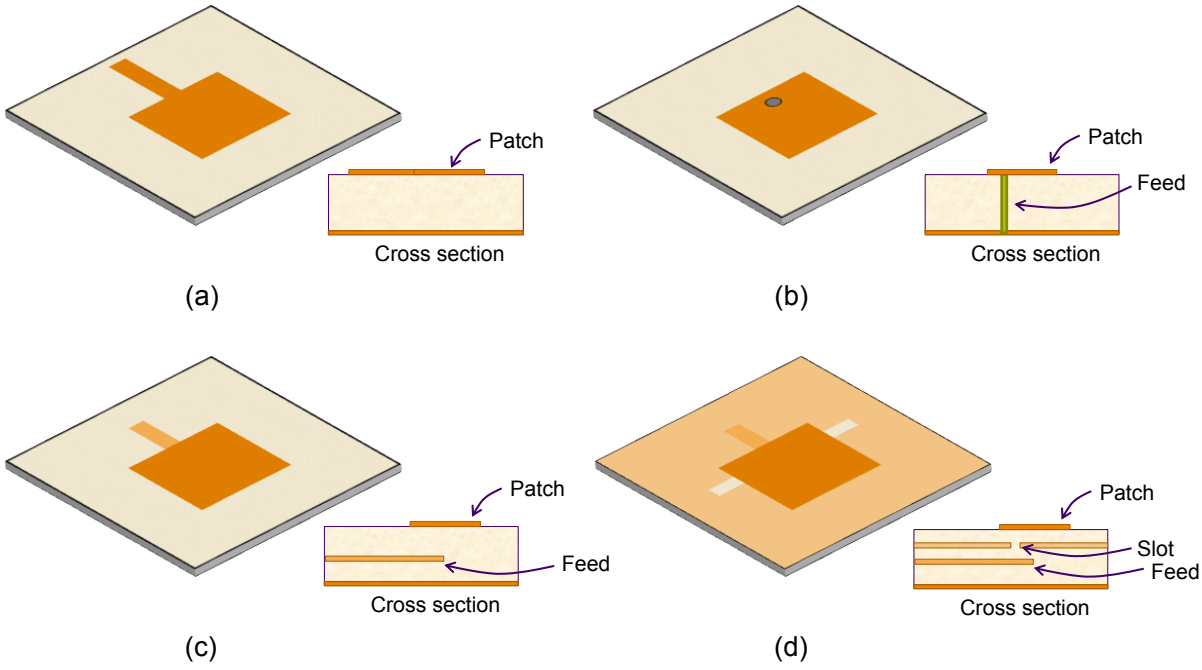

Figure 4.6: Feeding techniques: (a) edge feed, (b) coaxial feed, (c) proximity coupled, (d) slot coupled

4.3 Patch Antenna Design

There are several common patch antenna structures, each has its own advantages and disadvantages. The choice of which to use depends on the required antenna performance and the better integration to the rest of the radio system.

4.3.1 Common Patch Antenna Structure

The body of a patch antenna is an arbitrarily shaped metal trace which can be a rectangle, square, circle, ring, dipole, triangle, etc. Among these, the rectangle is the most popular due to its ease of design, analysis, as well as good cross-polarization performance [23].

The feeding technique of a patch antenna also has a great impact on RF performance. A straightforward option is edge feed (microstrip feed). As shown in Fig. 4.6a, a microstrip line is connected directly to the edge of the patch. This feeding technique is very easy to implement and tune, however, the bandwidth is relatively narrow, making it unsuitable for

5G mm-wave applications. An optimization technique can be added to this type of feeding structure to improve its bandwidth, which is to insert the feed into the patch (inset feed) [38]. Although it is shown the bandwidth is improved, the large footprint still forbids them from being used in an array setup.

Fig. 4.6b displays the coaxial feed of a patch antenna, where a via is connected to the patch serving as the feed path. This leverages PCB vertical integration capabilities and allows for a compact design. The bandwidth is wider compared to inset fed, but optimization can be done such as adding a parasitic layer to further increase the bandwidth. The small footprint makes it easier to integrate into an mm-wave antenna array. At lower frequency dual-polarization is easily achievable by coaxial feeds, however, due to the coupling between the two coaxial vias, it becomes harder to implement dual-polarization as the frequency increases [22].

Fig. 4.6c and d show proximity coupled and slot coupled patch antennas, respectively. Instead of connecting the feeding directly to the patch like in microstrip and coaxial feed, these two techniques use EM coupling to feed the antenna. The advantage is that the bandwidth is very wide, compared to the previous two techniques, however, the downside is they require multiple layers to implement because the feeding structure requires additional layers. The larger footprints pose difficulty in implementing in mm-wave arrays and are harder to implement as dual-polarization, but the wide bandwidth still makes them popular options.

The different types of patch antenna feeding and their pros and cons are summarized in Table 4.1.

Feed Technique	**Footprint**	**Bandwidth**	**Dual-pol**
Edge feed	Large	Very narrow	Easy
Inset feed	Large	Narrow	Easy
Coaxial feed	Small	Medium	Medium
Slot feed	Medium	Wide	Hard
Proximity feed	Medium	Wide	Hard

Table 4.1: Comparison of patch antenna feeding techniques

4.3.2 Coaxial Feed Patch Antenna Design

Coaxial feed structure is chosen for this project due to its compact size and ease of implementation, as well as the potential to scale to dual-polarization. For a patch antenna,

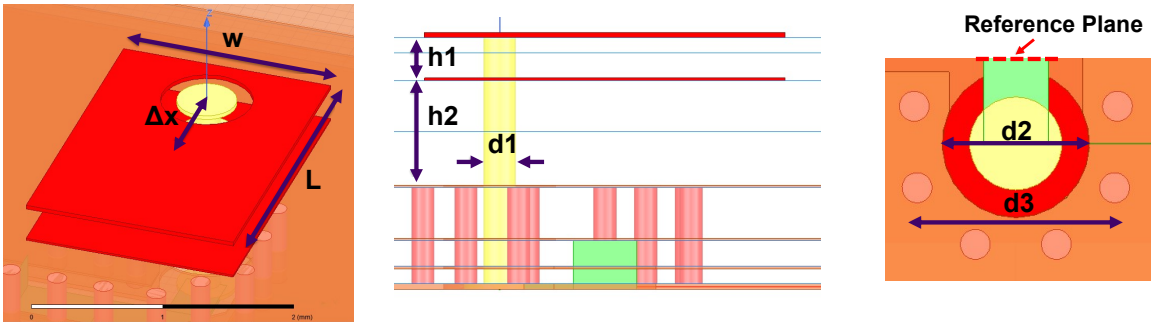

Figure 4.7: Coaxial feed patch antenna design parameters

its resonant frequency is dependent on its physical size, which can be roughly calculated using (4.1) [23]

$$F_{mn} = \frac{c}{2\pi\sqrt{\epsilon_r}}\sqrt{(\frac{m\pi}{L})^2 + (\frac{n\pi}{W})^2}, \tag{4.1}$$

where c is the speed of light, (W, L) is the physical dimension of the patch, and (m, n) are integers that determine the resonant modes. When a single polarization is used, one of m and n is zero, when both of them are used, the antenna is excited in circular polarization. From this equation, the dimension of a linear-polarized square patch antenna can be calculated. For Rogers RO4350B substrate with $\epsilon_r = 3.62$, the width of the patch is approximately $2.8mm$. This width can be used as a starting point to design the antenna. To avoid using a blind via, a through via is used in designing the stacked patches, shown in Fig. 4.7: the feeding via (yellow) is a through hole from the top layer to the bottom layer. As discussed in the previous section, a parasitic patch is added to the top of the main antenna to improve the performance. The main patch (lower) is placed on the third layer of the PCB, and the parasitic patch is placed on the top layer. The feed via, however, only connects to the main patch, therefore a ring is cut our from the parasitic patch to allow the through drill. The feeding trace as CPWG is fabricated on the bottom layer of the PCB, which connects to SMPM connectors.

The design parameter of the coaxial feed patch antenna are illustrated in Fig. 4.7, where W and L are the width and length of the patch antenna, respectively. These two parameters have direct effects on the resonate frequency of the antenna as discussed in (4.1). Δx is the coaxial feed offset distance from the patch center which changes the real impedance seen at the input port of the antenna. The input impedance for different Δx is plotted on a Smith Chart shown in Fig. 4.8. For the feeding coaxial via, $d1$ is the

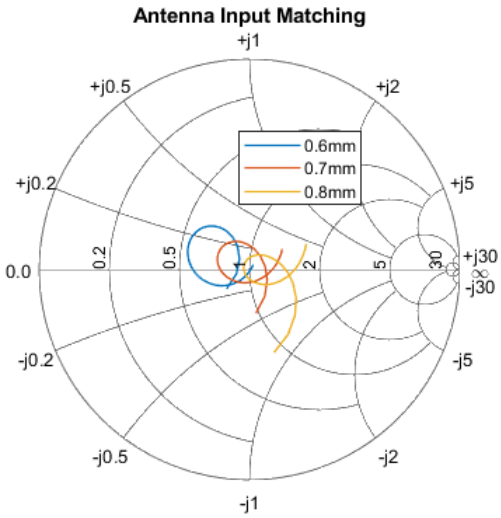

Figure 4.8: Antenna input matching (26-30 GHz) for different feeding position offsets.

diameter of the feed, $d2$ is the diameter of the ground hole, and $d3$ is the diameter of the via fencing diameter of the coaxial feed via. The feeding via and the via fence forms the coaxial transition, and their diameters control the impedance of this transition. From the reference plane point of view, the coaxial via acts as an impedance transformer, so they will have an impact on the antenna port input impedance. The simulation result for different via diameter and the fencing diameter are shown in Fig. 4.9a and b, respectively.

$h1$ is the substrate height between the main and parasitic patch, and $h2$ is the substrate height between the main patch and the antenna ground. Note that these two parameters depend on the PCB stack up and dielectric material availability, for example, Rogers RO4350B is only available in a few thickness (e.g. 4 mil, 6.6 mil, 10 mil, etc.) pre-defined by the manufacture. They also depend on the arrangement of PCB core (RO4350B) and prepreg (RO4450F), for example, two layers of prepreg (8 mil in total) must be used between two cores, and a blind via must start from core layers. These dependencies limit the flexibility of the antenna design, especially on the antenna bandwidth.

Overall, these design parameters are optimized together to achieve wide bandwidth of operation, as well as a low level of mutual coupling between antenna elements in the array. The design parameters of the patch antenna are listed in Table 4.2.

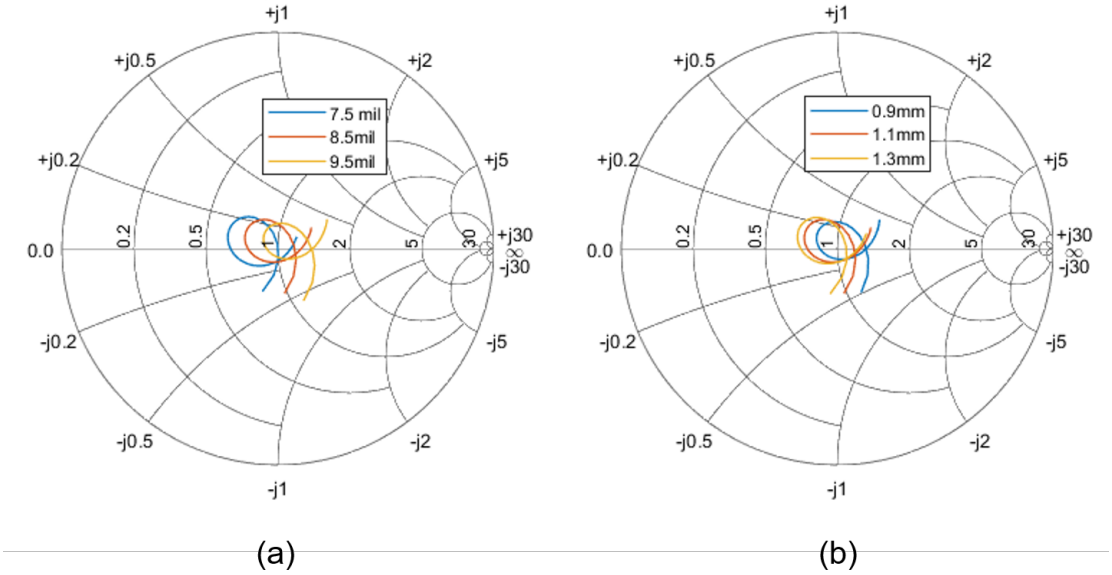

Figure 4.9: Antenna input matching (26-30 GHz) for different (a) feeding via diameters and (b) via fencing diameters

Parameter	Description	Value	Unit
W	patch width	1.7	mm
L	patch length	2.4	mm
Δx	feed via offset	0.7	mm
h1	height between primary and parasitic patch	12.67	mil
h2	height between primary patch and ground	25.3	mil
d1	feed via diameter	8.5	mil
d2	feed ground hole diameter	28.5	mil
d3	feed via fencing diameter	1.1	mm

Table 4.2: Summary of patch antenna design parameters

4.4 Near-Field Probing Array

The near-field probing array is the essential functional building block in this RF beamforming array, which is responsible to receive the transmitted signals from all beamforming elements, with equal weight, so the received signal can be used for array calibration and DPD.

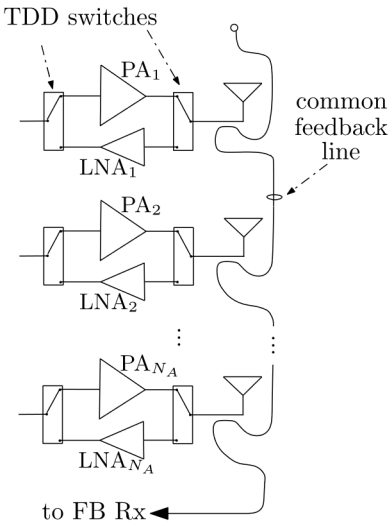

Figure 4.10: Shared feedback implementation [37]

4.4.1 Viable Coupler Implementation

There are many ways to implement a structure that can receive the transmitted signals. A few options are:

1. inserting a coupler which couples to the antenna feed.
2. inserting a resistive coupler between the PA output and the antenna feed.
3. adding additional antennas which couples to the beamforming antennas through mutual coupling.

In the first case, it is applicable to implement the coupler as a coupled line couplers at mm-wave frequencies [37]; but they consume too much space and are not practical for a planar array. For a resistive coupler, it can be inserted between the PA output (port 1) and the antenna (port 2) to provide coupled transmitting signals, as illustrated in Fig. 4.11. While it is easy to implement using embedded resistor technologies and easy to control the coupling factor (by tuning the resistor values), it is undesirable that the resistors make it lossy.

The mutual coupling based implementation gained popularity in recent years. One of the advantages is that the mutual coupling happens between all antenna elements, therefore

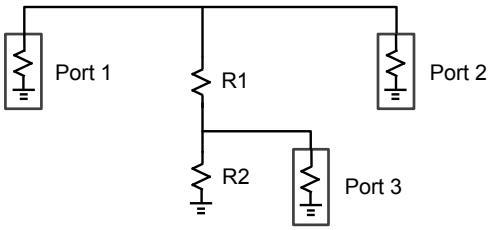

Figure 4.11: Resistive coupler schematic

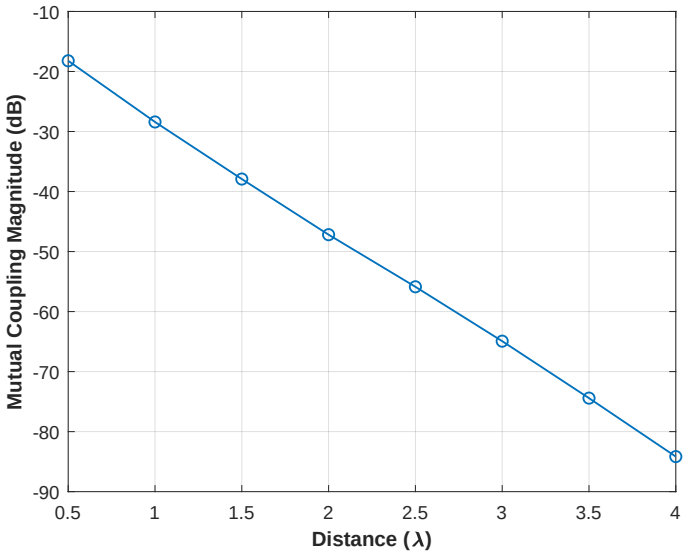

Figure 4.12: Antenna mutual coupling vs. distance simulation.

only one antenna, defined as a probe, is required to couple to all others. However there are practical constraint when using only one probe: the mutual coupling strongly depends on the distance between the elements. To illustrate this, a simulation is conducted for two antennas spaced with various distance apart, and their mutual coupling is displayed in Fig. 4.12. As a result, for a large array, one probe is not sufficient, and an array of them is needed.

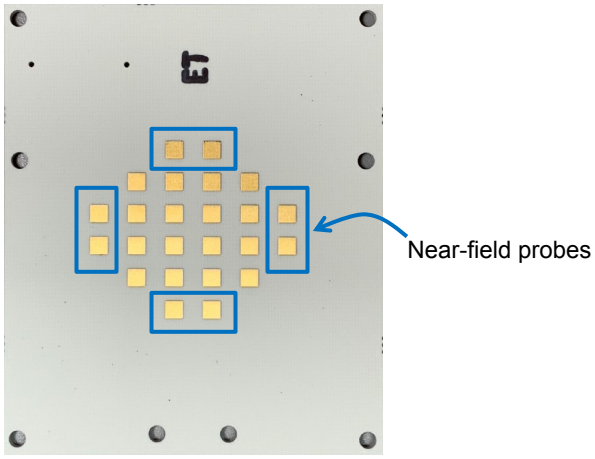

Figure 4.13: Near-field probes are placed on array perimeters, in [34]

4.4.2 Near-Field Probing Array Design Requirements

1. **Uniformity**: the near-field based TOR relies on the mutual coupling between array radiating elements and the near-field probe elements, since the mutual coupling magnitude strongly depends on the physical arrangement of the array, as illustrated in Fig. 4.12, a suitable layout is needed such that the mutual coupling between each radiating element and at least one element of the near field probing array has similar magnitude. This is to ensure a similar signal-to-noise ratio (SNR) of the coupled signal for all radiating elements.

2. **Modularity**: the design of the beamforming array with the near-field probes must be suitable for any array size. This requirement along with the uniformity requirement disqualifies most of the existing array designes covered in the literature review. For example, in [34] and [21], the probes are placed on the perimeter of the radiating array, shown in Fig. 4.13. This approach is very simple to implement, however, not only the mutual coupling magnitude varies for different elements, but also the elements at the center region of the array are very far from any of the probes, which result in low SNR that can degrade calibration and DPD performance. Therefore both the uniformity and modularity requirements are not met.

   In another approach, authors in [20] put Rx elements in a grid, surrounding the Tx elements, and use the Rx elements as near-field based TOR. This implementation is appealing because no additional receiver hardware is needed for probing, and it satisfies the modularity requirement. The downside is for this approach is that the

Tx and Tx elements are separated, making the array naturally bigger, and sacrifices Rx element spacing. Besides, the Rx elements are not uniformly distributed between the Tx elements, making the mutual coupling non-uniform.

3. **Flat coupling frequency response**: DPD engine training requires a wide-band signal, typically several times the signal modulation bandwidth. Since the modulation bandwidth for 5G mm-wave is in the order of hundreds of MHz [2], the mutual coupling between the radiating elements and the probe elements needs to be flat over at least two GHz around the center frequency.

4. **The addition of the probes must not disturb beamforming performance**: since the near-field probes operates based on mutual coupling, it can easily change the EM characteristics of the beamforming array elements, so the conglomeration of the beamforming array elements and the near-field probe elements needs to be optimized that there is no significant beamforming performance degradation.

5. **Impedance matched**: since the near-field probe is connected to a receiver for demodulating, there can be impedance mismatch between the receiver and the near-field input port. This can be an issue since impedance mismatch will cause reflection between the probe and the receiver, thus degrading the received signal quality. Therefore the input impedance of the near-field needs to be matched to the receiver's system impedance.

To satisfy the design requirements listed above, a new embedded near-field probing array is designed.

4.4.3 Design of Near-Field Probe

Because of the modularity and uniformity requirements, the probe is selected to be placed in center of 4 beamforming elements, illustrated in Fig. 4.14. This ensure the symmetry in a 4-element unit cell, which makes the coupling magnitude and phase between any of the 4 beamforming element and the probe to be equal. Note that the feeding of the second-row beamforming elements are rotated 180° to further improve this symmetry. The beamforming elements have a spacing of 5.4mm (0.5λ at 28 GHz) in both x and y axis to achieve optimal beamforming capability without grating lobes.

The near-field probe is designed following a similar structure as a coaxial feed patch antenna. It is also designed to be symmetrical so that the complete unit cell is also

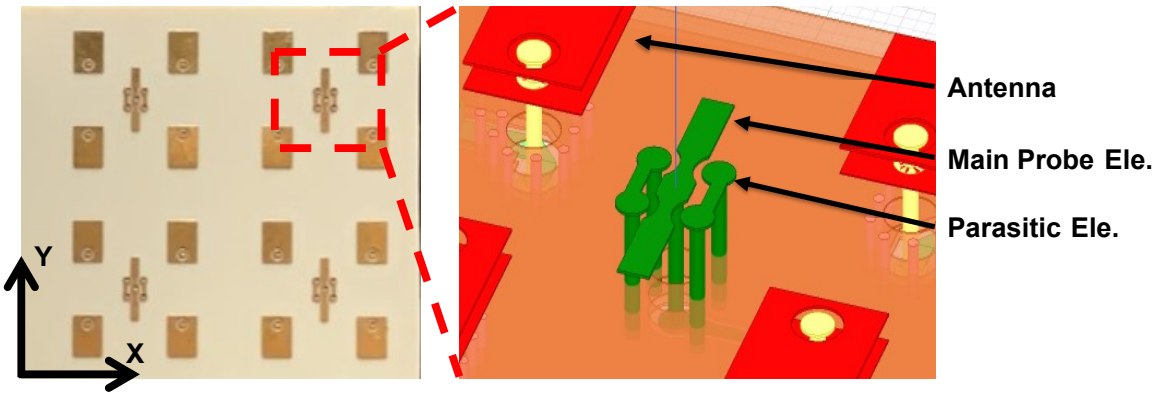

Figure 4.14: Near field probe integrated with beamforming antenna array

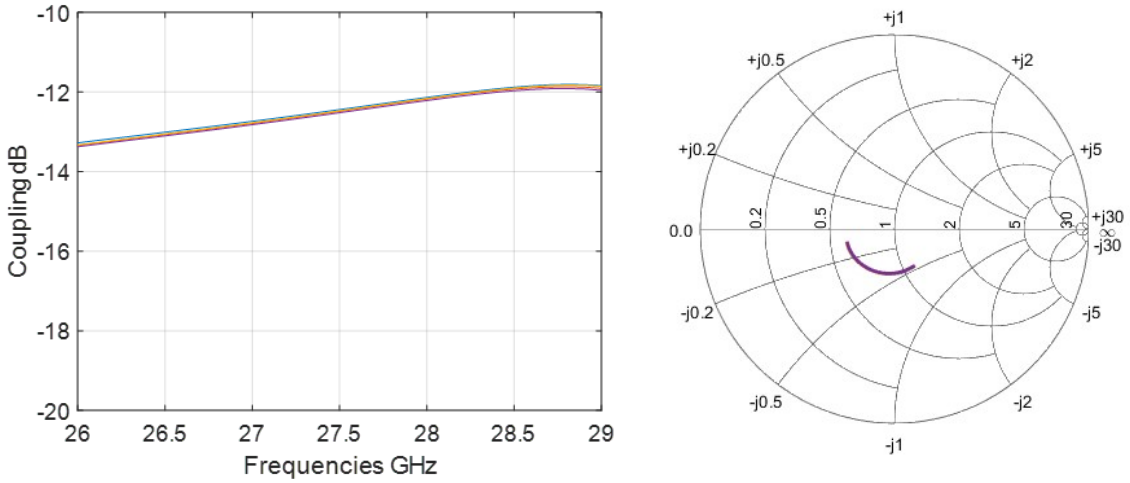

Figure 4.15: (a) Near-field probe coupling magnitudes to the four antenna elements, over 3 GHz band; (b) Coupling magnitude and phase for the four antenna elements.

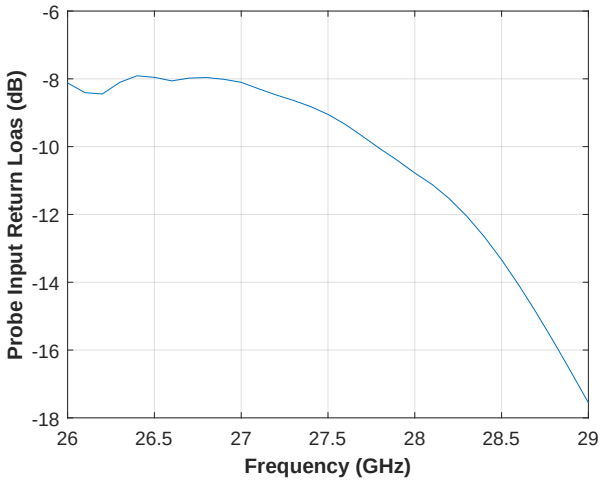

Figure 4.16: Input return losses of near-field probe (acceptable matching at the desired band, but shifted towards higher frequency)

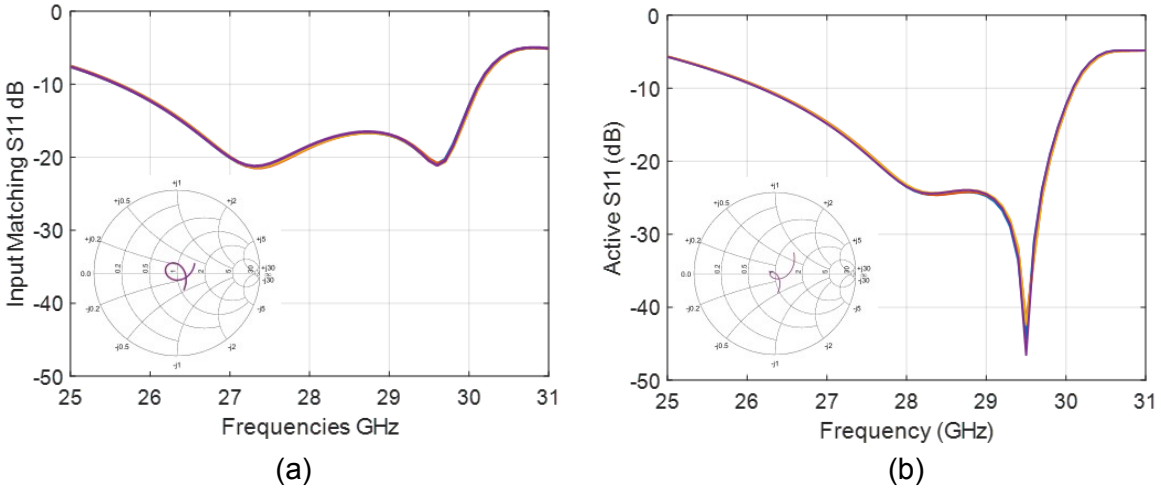

Figure 4.17: (a) Input matching (S11) of the four elements in the unit cell; (b) Active S11 of the unit cell at boresight.

symmetrical in both x and y axes. The probe consists of two structures, the main body and a parasitic element; the main body has a shape similar to that of the coaxial fed patch antenna, with the feeding via in the center, and is shaped much smaller than a beamforming element. The parasitic element connects the via pads of the surrounding ground vias, which improves the input matching of the probe. The dimension of the probe is optimized with the beamforming array in HFSS to achieve wide bandwidth of operation.

In a four-element unit cell, which has four beamforming antennas and one near-field probe, the coupling magnitude between the 4 beamforming elements and the probe is displayed in Fig. 4.15a, which proves that the designed probe couples to the antenna elements over a wide frequency band. The phase of the coupling between the elements is also equal, shown in Fig. 4.15b in a smith chart from 26 to 29 GHz. The input matching of the near-field probe is difficult to achieve because of the desired footprint. Although parasitic elements are added for this purpose, it still has disadvantages over a regular antenna. As displayed in Fig. 4.16, the worst point is -8 dB, and it is better matched at higher frequency thanks to the parasitic elements, without which the return loss is near -4 dB across the band. With the addition of the near-field probe, the beamforming antenna design parameters also need to optimized, Fig. 4.17a displays the input matching of the 4 antenna elements with -10 dB bandwidth of over 4 GHz, centered at 26-30 GHz. The active S11 at the boresight of the 4-element unit cell is also analyzed and displayed in Fig. 4.17b. The radiation efficiency of the designed antenna is around 95% from 26 to 29 GHz, and drops to 79% at 30 GHz. Overall, the design process of the unit cell follows Fig. 4.19.

4.5 16-Element Planar Array and Stack Up

The stack up of a mm-wave beamforming array integrated with RFIC and patch antennas are typically determined by the antenna structure, this is because the patch antennas require thick substrate and potentially blind vias for connecting the ground, so 4 to 8 PCB layers are typically required. To facilitate the RF signal routing, RF shielding, power delivery and digital control routing of the RFIC, an additional 4 to 8 layers, and one or two blind vias are needed. Thus, the overall stack up will have 8 to 14 layers with minimum of 2 to 3 blind vias, listed in Table 4.3.

There are three ways to build a blind via in a PCB:

1. by laser drill (micro via): same as in an HDI stack up, laser drill can be used to drill through a maximum 2 layers or 10 mil.

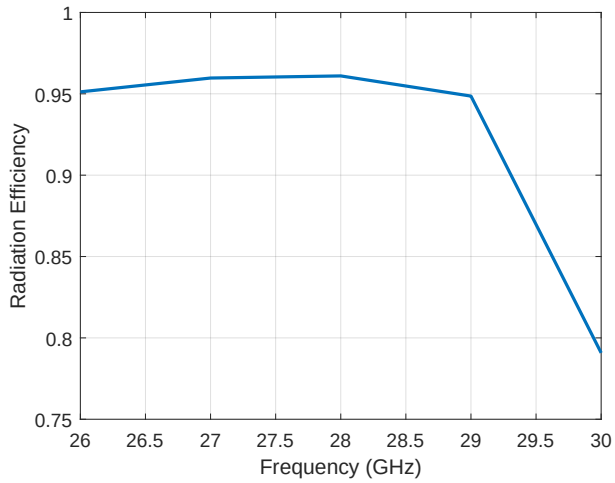

Figure 4.18: Radiation efficiency of the patch antenna.

Num Layers Required	**Function**	**Blind Via**
4-8	Patch antenna	dedicated
2-4	Digital signal routing	shared
1-2	Power plane	shared
1-2	RF common (for beamforming)	dedicated
1	RF common (for near-field probing)	dedicated
1-2	Ground shielding	shared

Table 4.3: Summary of patch antenna design parameters

2. by multi-lamination: in each lamination cycle, a through hole is drilled, then the next lamination is applied on top of it, making it a blind via.

3. by drilling a through hole followed by back drill. This is illustrated in Fig. 4.20, a through hole is first drilled in the PCB, then a wider controlled-depth drill is applied on this via to remove any coppers in unwanted layers. Epoxy is then added to to fill the hole, and the left-over via becomes a blind via. The advantage of the approach vs. multi-lamination is that the cost is much lower, and the common layer only needs to be plated once. However, the depth control of the drill usually has a tolerance of 10 mil, so the blind via may have a stub of a maximum 10 mil. The most critical disadvantage in an antenna stack up is that the back drill will leave holes in the layers it drills through. For example, the second layer in Fig. 4.20 is used as antenna

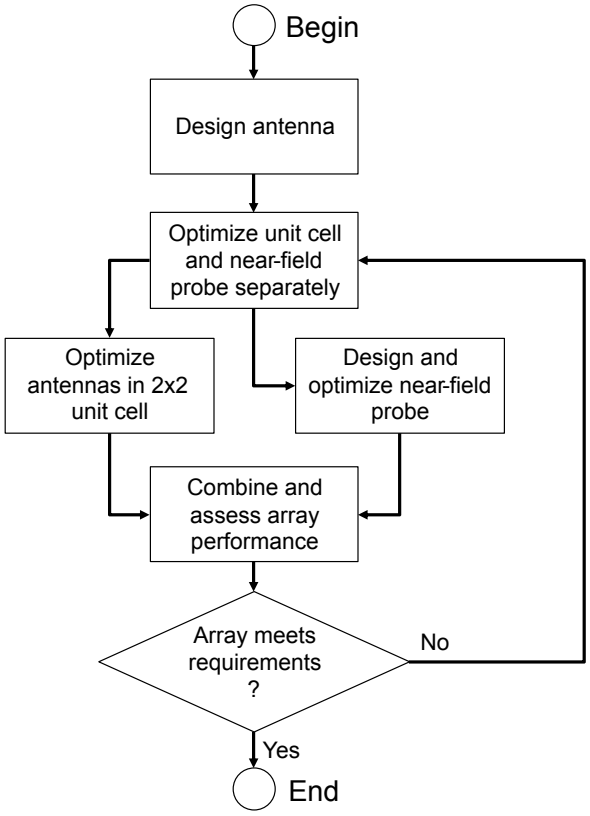

Figure 4.19: Design process of beamforming phased array with integrated near-field probe.

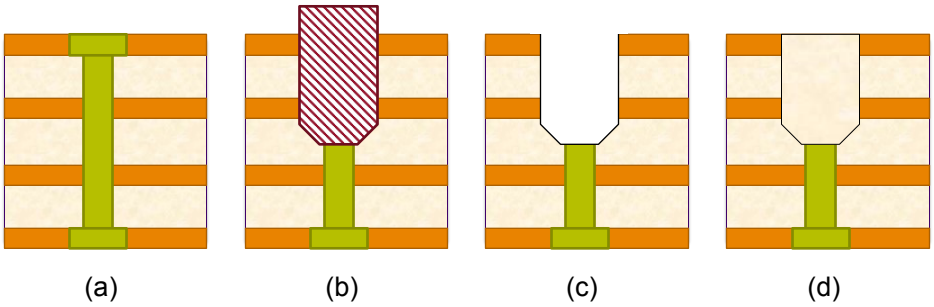

Figure 4.20: Process of back drilling: (a) start with a plated through hole, (b)-(c) a wider drill is applied to remove copper from unwanted layers, (d) the back drilled hole is filled with epoxy. There is an unwanted stub left over due to back drill tolerance.

ground, if the blind via is drilled using back drill, then there will be a hole on Layer 2, causing the antenna ground to be non-continuous, introducing potential antenna performance degradation.

Examining the listed methods, multi-lamination is selected to be the process to build the RF beamforming array. The substrate thickness for the antenna that is compatible with RO4350B/4450F is 37.3 mil, which requires 3 sheets of material between the main and parasitic patch, and 5 sheets between the main patch and ground. Note that not all layers between the sheets are needed: shown in Fig. 4.21.

The near-field probe poses another challenge in stack up implementation: the RF traces for the near-field probes need to go from the antenna layer to below antenna ground, then be routed in a different layer than the RFIC. For example, in Fig. 4.21, these traces need to be routed on one of L6, L7, and L8. The via needs to be implemented as a blind via from L1 to L6-8. This is not possible for a multi-lamination process, and can only be achieved by back drill. To lower the risk associated with combining multi-lamination and back drill, the stack up is split into two:

- **Primary stack up**: an 8-layer multi-lamination stack up built for the antennas and near-field probes. The traces of the near-field probes are routed by a through hole via, then on the bottom layer of the PCB. The antenna feed vias are also drilled as a through hole via. Antenna ground vias are implemented as blind vias.
- **Secondary stack up**: the same 8-layer stack up built for mounting the RFIC and routing digital control signals and power layers.

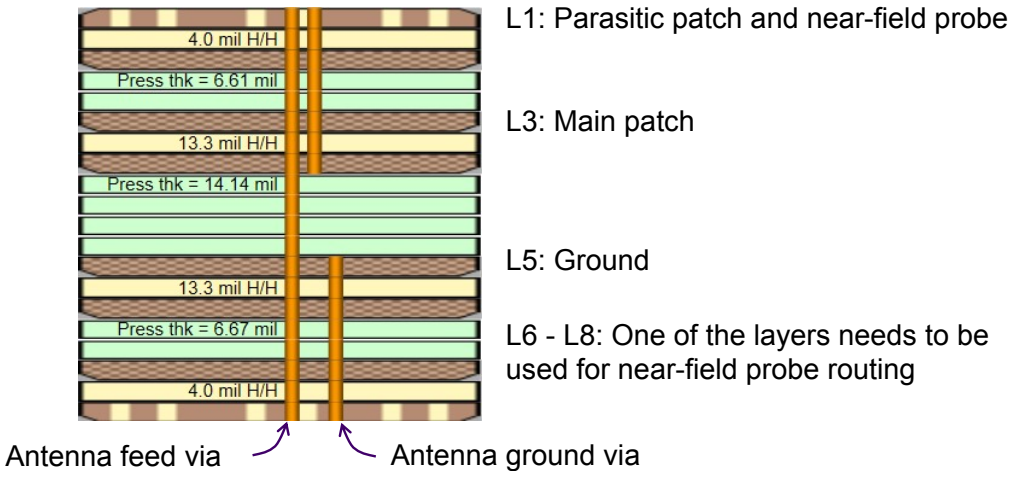

Figure 4.21: Proposed symmetrical antenna stack up.

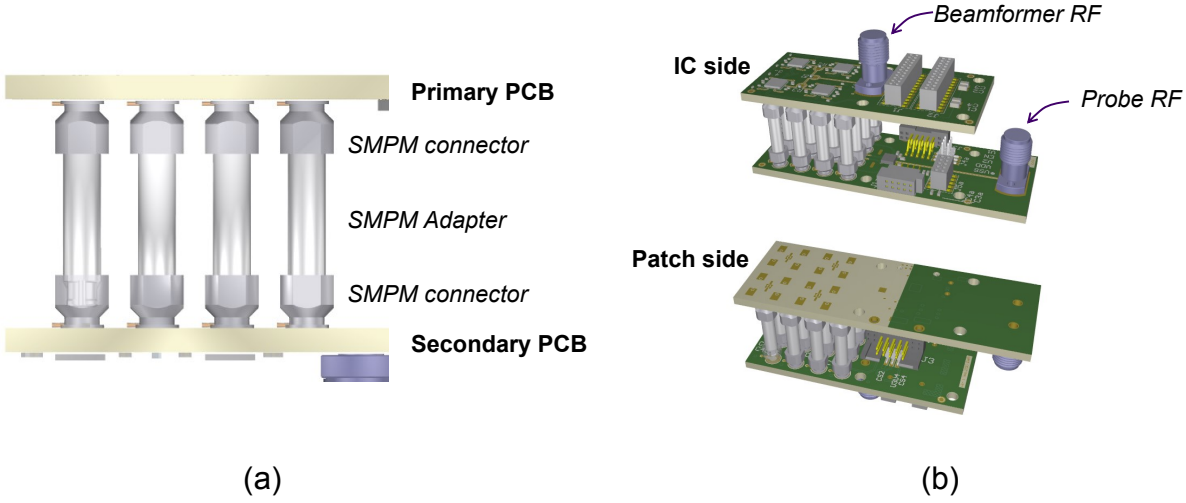

Figure 4.22: Assembly of the primary and secondary PCB with SMPM adapters

Note that the two stack up are kept the same to lower the production cost, as the two are manufactured at the same time. The stack up is also a symmetrical built with symmetrical blind vias, which allows the top and bottom half to be built at the same time, further reducing the cost. The disadvantage of the two-stack-up implementation is that the two PCBs have to be connected together. This is done by using low-profile SMPM connectors and adapters, illustrated in Fig. 4.22a. Another reason why the stack up is divided into two is that the near-field probe feeding via is drilled at the center of the 4 surrounding elements, where the RFIC is mounted. This blind via is possible in a more complex multi-lam stack, but to minimize the risk associated, the separated stack up is chosen.

The 4×4 array is put together by 4 2×2 unit cells, therefore there are a total of 4 near-field probes. The probes feedings are routed on the bottom layer of the primary stack up and are connected to a single-pole qual through (SP4T) switch, making a single output for the near-field probing array. The overall assembly of the 4×4 beamforming array displayed in Fig. 4.22b

The Anokiwave AWMF-0162 qual core beamforming RFIC is used for this project. The chip uses wafer level chip scale package (WLCSP) with a ball pitch of 0.4mm. The dimension of the RFIC is 3.6×3.6 mm. For a WLCSP IC, its landing pattern on the PCB is important to its reliability, thus consideration needs to be made on the pad implementation. Because the PCB is a built in a multi-lamination process, the outer layer finished copper is thick (2oz), therefore soldermask-defined (SMD) pads are preferred over non-soldermask-defined (NSMD) pads for ground connection [30]. However, the IO pads are implemented using NSMD to ensure the solder will flow in the pad area and firmly attached to the pad. The pad dimension and the solder mask opening is displayed in Fig. 4.24, all pads opening have the same diameter of 10.5 mil, and the NSMD pads are slightly smaller than the opening.

The IC uses serial peripheral interface (SPI) for digital control and a single external 1.8V power rail. The DC power is delivered to the RFICs through two power planes, which are implemented in two of the middle layers. The SPI is routed as a 2-IC daisy chain, where the 4 ICs are divided into 2 groups, and each group shares the same *chip select* signal. The digital signals and power are supplied through two 24-pin, 50-mil pitch connectors. Fig. 4.23 shows the secondary PCB layout.

The 4×4 beamforming array layout is designed to have a width of 21.6mm (2λ at 28 GHz), because the beamforming element spacing is 0.5λ, multiple 4×4 arrays can be put together to form a larger array with the same element spacing, for example, Fig. 4.25 shows an 8×8 array built using 4 4×4 sub-arrays.

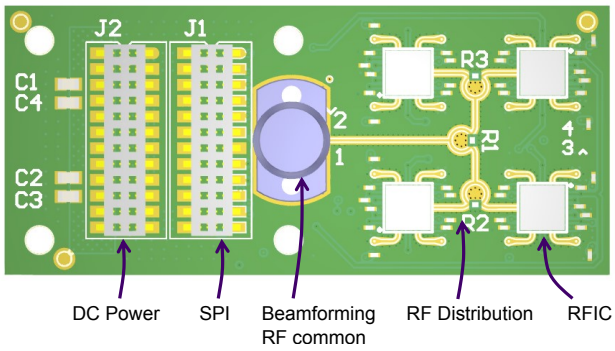

Figure 4.23: Layout illustration of the secondary PCB of the 16-element beamforming array.

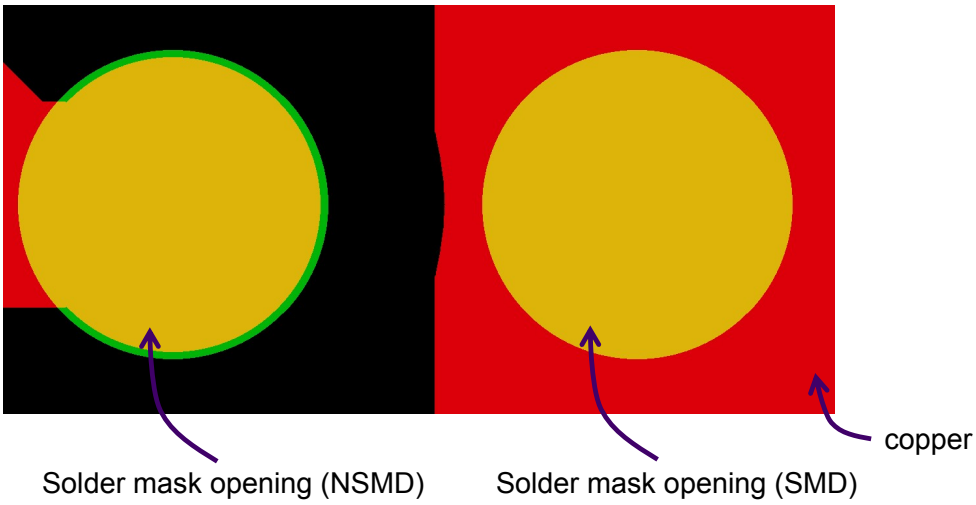

Figure 4.24: Both SMD and NSMD pads are used for secure attachment of the RFIC

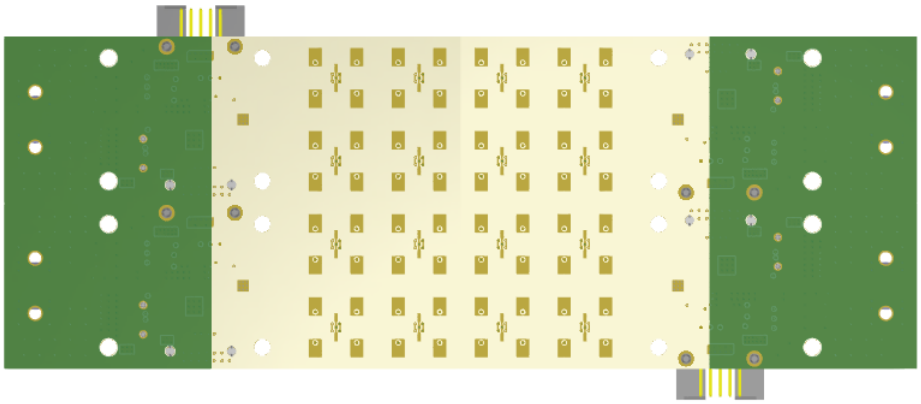

Figure 4.25: 8×8 beamforming array with 16 near-field probes assembled from four identical 4×4 subarrays.

4.6 64-Element Planar Array and Stack Up

Besides the 16-element beamforming array, a 64-element array with similar near-field probes are also designed to facilitate use cases of large-scale hybrid beamforming application which uses up to 256 antenna elements. The 64-element array is designed after the learning cycle of the 16-element array, therefore a new stack up is used, but the rest of the design remains largely the same.

One of the issues in the dual-PCB design is that the adapters connecting the two PCBs are lossy, which is critical because it serves as the connection between the RF front-end and the antenna - any losses in this connection should be minimized to achieve the best noise figure and highest transmitting power. To solve this issue, a new multi-lamination stack up is proposed which is based on the original 8-layer design. As shown in Fig. 4.26, the 10-layer stack is divided into two sub-stacks: L1-L4 and L5-L10. The upper stack houses the stacked coaxial fed patch antenna on L1 and L2, with ground reference on Layer L3. As discussed in the previous subsection, the near-field probe RF routing must be done below the antenna ground, thus L4 is designated as a stripline layer for it, and it is connected to the probe through a through via. The lower stacks are used for digital control signal routing and power delivery. The two stacks are bonded together using I-TERA prepreg material, and the grounds of the two stacks are connected using Ormet sintering paste such that the upper stack microvia and the lower stack through vias are connected together [19]. The stack up material except the sintering layer are Astra MT77, which is a premium low-loss material targeted for mm-wave applications.

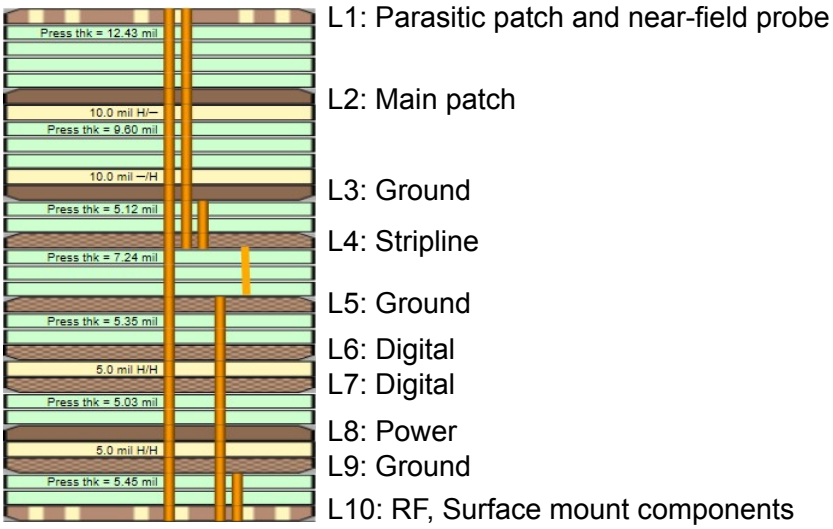

Figure 4.26: 10-layer stack up used for 64-element array.

There are 16 near-field probes for the 8×8 beamforming array, they are placed at the centers of every 4-element unit cell. The 16 probes are connected to 5 SP4T switches such that they share one common RF port. Dummy antennas are placed around the array to improve edge element performance. Fig. 4.27 shows the IC and antenna side of the PCB.

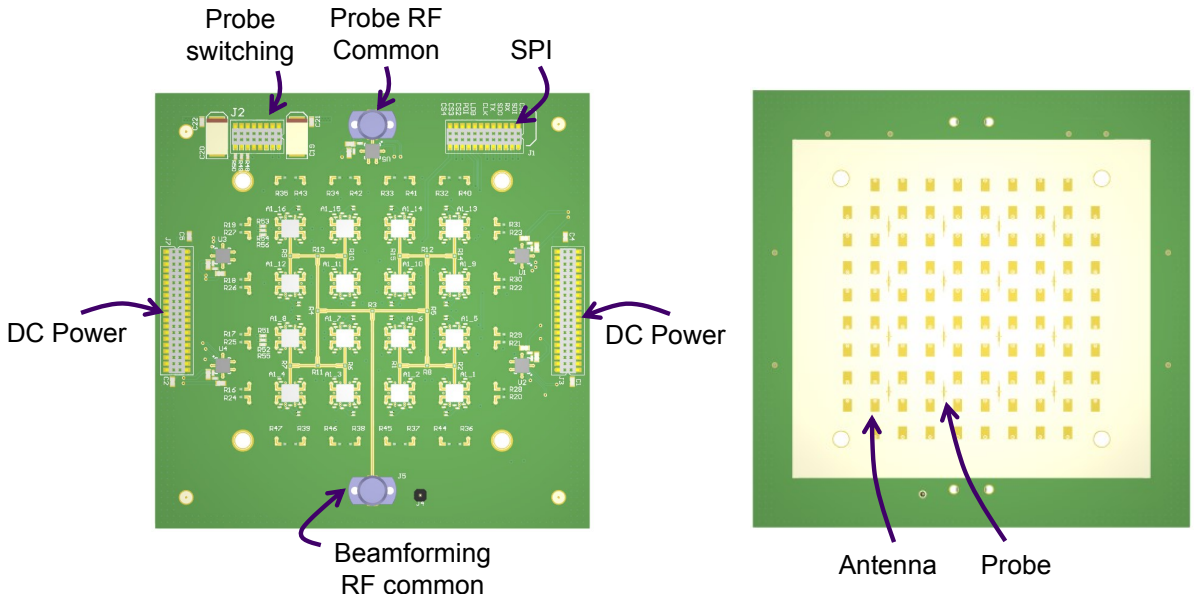

Figure 4.27: Layout illustration of 64-element beamforming array with 16 near-field probes.

Chapter 5

Experimental Validation

The 16-element 4×4 beamforming array with integrated near-field probes is fabricated and assembled for experimental validation.

5.1 Antenna Passive Measurements

As the primary design module, the antenna PCB is measured using a VNA to verify antenna and near-field probe designs. Fig. 5.1 shows the measured input matching of the designed antennas (SMPM connectors are de-embedded). Because of the narrow padding of the array, each antenna element exhibits different boundary conditions and the performance is slightly different too. It is noticed that there is a frequency shift of the antenna center frequency, from 28 GHz to 29 GHz. This is due to the non-ideal modelling of the surface finish during the design stage: the finished PCB outer layer copper thickness is underestimated, which introduces unexpected parasitic that shifts the antenna frequency.

Fig. 5.2 shows the s-parameter measurement of the near-field probe: the coupling (S21) between the near-field probe and the antenna. There are 16 beamforming antennas and 4 probes in total, in Fig 5.2a, coupling between one of the probes and the 16 antennas is measured. Group A highlights the 4 antennas that are surrounding the chosen probe. Fig 5.2b displays the coupling between all antenna elements and their respective nearest near-field probes. This figure shows that the magnitudes are mostly constant across the frequency band and that the coupling magnitudes are close for all probes. These results verified that the design of the antenna and the near-field probes function as intended.

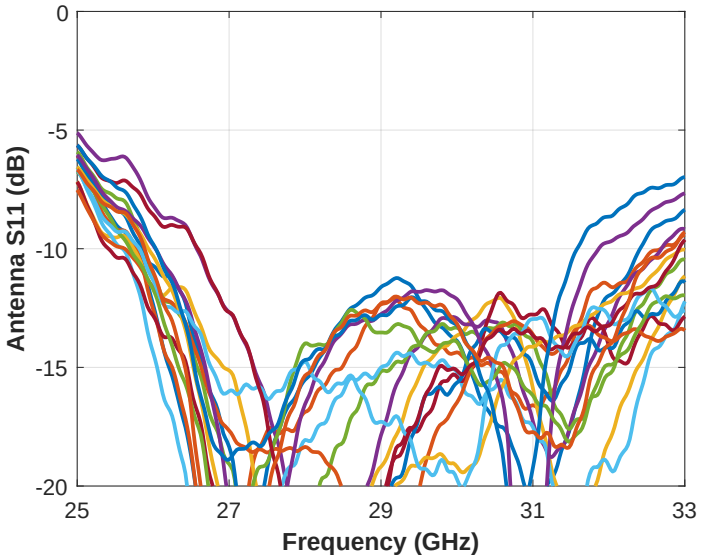

Figure 5.1: Input matching (S11) of the 16-element beamforming antenna.

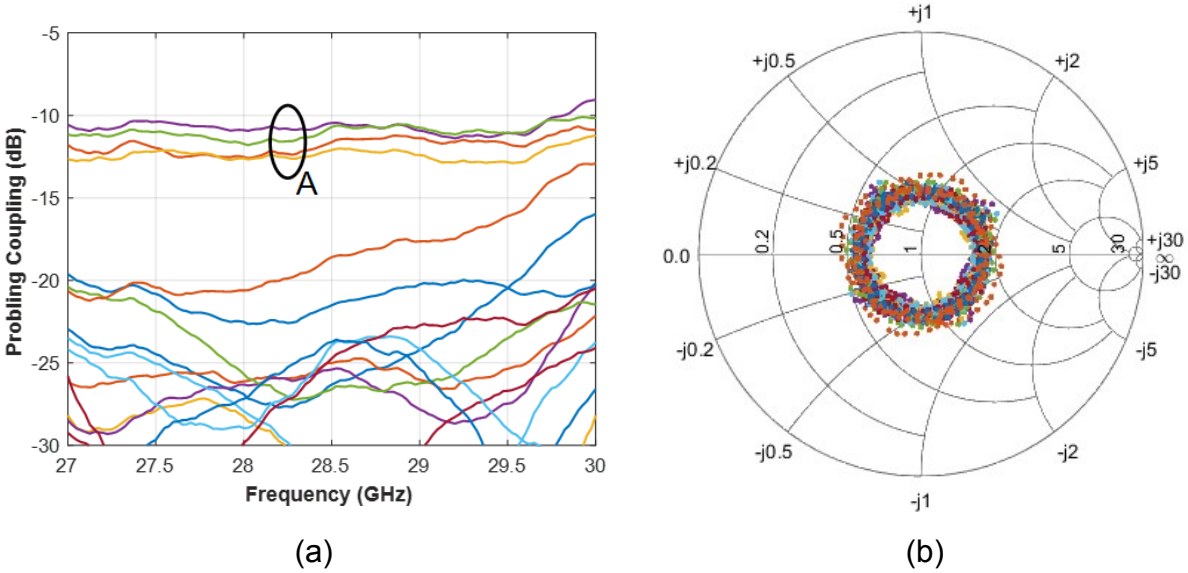

Figure 5.2: Near-field probe to antenna coupling measurement results: (a) between one of the near-field probes and the 16 elements, (b) between the four near-field probes and the 16 elements.

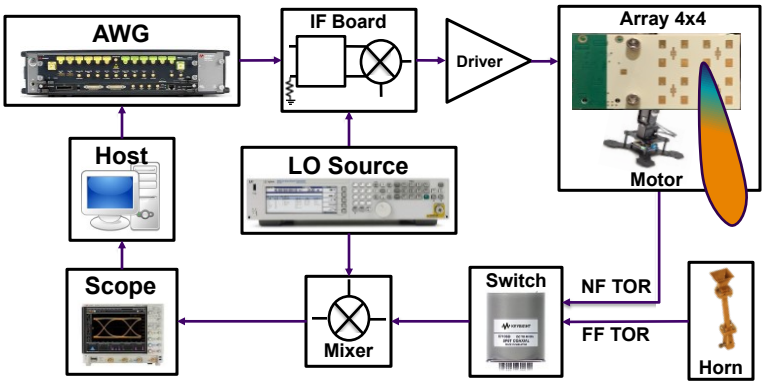

Figure 5.3: Measurement setup for beamforming array

The antenna PCB is connected to the beamforming IC PCB through SMPM connectors and adapters which are lossy. The measured loss of this transition is 1.9 dB maximum including the adapter and the 2 connectors. This implies that the antenna input matching, as well as mutual coupling between elements, are improved.

5.2 Beamforming Array Performance Assessment

Based on the theory developed in Chapter 3 which concluded that the beamforming array can be calibrated using the near-field probes, the fabricated array is put to test to verify this claim. The measurement is carried out in a setup pictured in Fig. 5.3, where the IF signal is generated using an arbitrary waveform generator (AWG), fed into a hybrid coupler with an IQ mixer for upconversion. The up-converted RF signal is amplified and then fed into the beamforming array. A far-field receiver probe is put at the boresight of the array, both the far- and near-field probes are connected to a switch, and the common path is down-converted and collected by an oscilloscope. The local oscillator (LO) signal for both up and down-conversion is generated from a signal generator.

In the array calibration test, two test signals are used: single tone (CW) and 400MHz OFDM signal with 11dB PAPR. Fig. 5.4 displays the amplitude and phase root-mean-square (RMS) variation between 16 channels before and after calibration vs. phase shifter settings (6 bits, 64 states): the test signals used in each test case are listed in Table 5.1. Before calibration, the array has 1.19dB - 1.33dB RMS Tx amplitude and 12.2° - 13.1° phase variation. After calibration, this variation is reduced significantly, in the worst case (cal 4), the variation is reduced to 0.21dB- 0.41dB and 1.75° - 4.09° for amplitude and

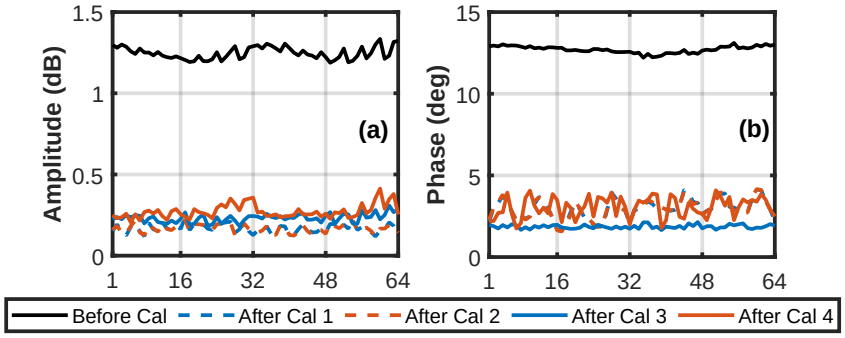

Figure 5.4: Array element rms variation before and after calibration for: (a) amplitude, (b) phase.

phase, respectively. Results for other cases are listed in Table 5.1. From the result, it is validated that the near-field probe can be used for array calibration, and the result is on par with or only slightly worse than that using far-field probe.

Test	Test signal	TOR	After cal variation (average)
Cal 1	CW	Far-field	0.17dB, 2.96°
Cal 2	CW	Near-field	0.17dB, 2.96°
Cal 3	400-MHz OFDM	Far-field	0.23dB, 1.86°
Cal 4	400-MHz OFDM	Near-field	0.27dB, 3.06°

Table 5.1: Array calibration test cases and results

When the array is calibrated, the array radiation pattern is measured using a CW signal. The antenna array is attached to a motor turning in the azimuth plane, and the far-field probe is fixed at around 60 cm away from the antenna. Displayed in Fig. 5.5, the array is capable of scanning to $\pm 50°$ without significant side lobes. The non-ideality and imbalance of the radiation pattern are attributed to the small grounding and the asymmetry.

5.3 DPD Measurements

Besides enabling near-field based array calibration, another important use case of the near-field probes is DPD. The theory was developed in [5] which verified the possibility of linearizing PAs using DPD techniques with near-field based TOR. In [18], the author

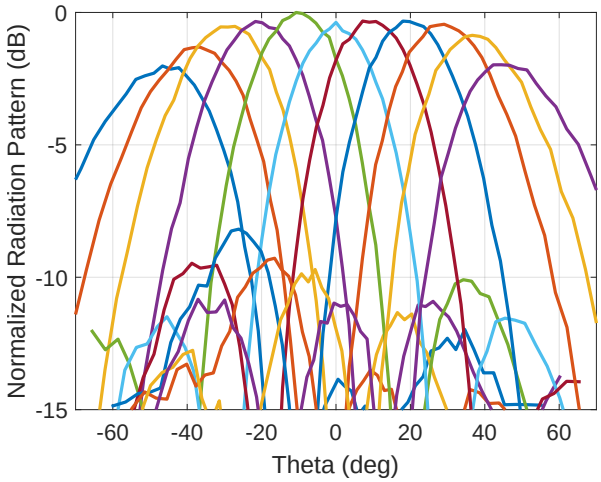

Figure 5.5: 4×4 beamforming array radiation pattern measurement results

developed a theory where symmetrical near-field feedback within an array is employed to linearize the PA but did not provide a viable solution to implement such array at mm-wave frequency. In [4], the author successfully linearized the PA using the proposed array with near-field probes at mm-wave frequency.

The same measurement setup depicted in Fig. 5.3 is used in DPD measurements. The test signal is a 400-MHz OFDM signal with 11dB PAPR and subcarrier modulated using 256 QAM. Fig. 5.6 shows the ACPR and EVM results at the far-field probe versus EIRP: (a) prior to DPD; (b) after DPD was trained using far-field based TOR [24]; (c) after DPD was trained using near-field based TOR with a presynthesized DPD target signal [5]; (d) after DPD was trained using the NF-based TOR with the array phase shifter settings adjusted to achieve coherent combining of the signals at the NF probes [18]. From Fig. 5.6, it is evident that the DPD trained using the near-field based TOR achieved similar results to the DPD trained using the far-field based TOR. ACPR and EVM improved from 30 dB and 8.8% before DPD to 38 dB and 2.9% in (b, c), and 39 dB and 2.5% in (d), respectively, when the array EIRP was set to 33 dBm. It is interesting to note that, using DPD, the EIRP increased by 5.5 dB from 27.5 dBm to 33 dBm while remaining below the maximum 3.5% EVM requirement. One of the interesting features of the proposed near-field probe is that the coupling between the antenna elements and the nearest near-field probes are uniform and flat versus frequency. This is critical for the performance of the near-field based DPD in (d), as the uniform coupling ensures coherent combining at the near-field probes (mimicking the signal combining at the far-field probe) resulting in similar linearization

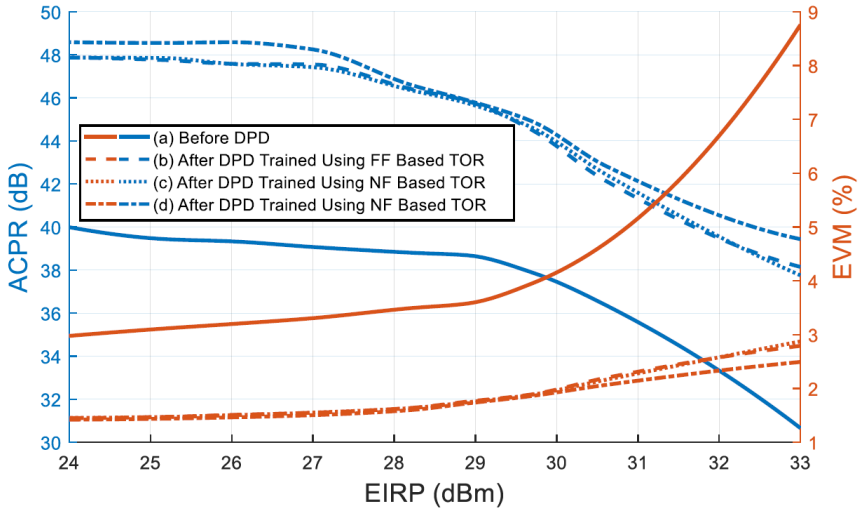

Figure 5.6: Near-field based DPD assessment: ACPR and EVM vs. EIRP (a) before DPD, (b) after DPD trained using far-field based TOR [24], (c) after DPD trained using near-field based TOR [18], (d) after DPD trained using near-field based TOR [5]

performance to the reference far-field based DPD training.

The second test is conducted using the new near-field based DPD training algorithm [4], where the near-field channels between the probes and the antennas are estimated and used to predict the far-field signal for DPD training. The result is displayed in Fig. 5.7. It is shown that ACPR and EVM improved from -29.66 dB to -40.49 dB and 8.29% to 2.40%, respectively, proving the validity of the theory and design.

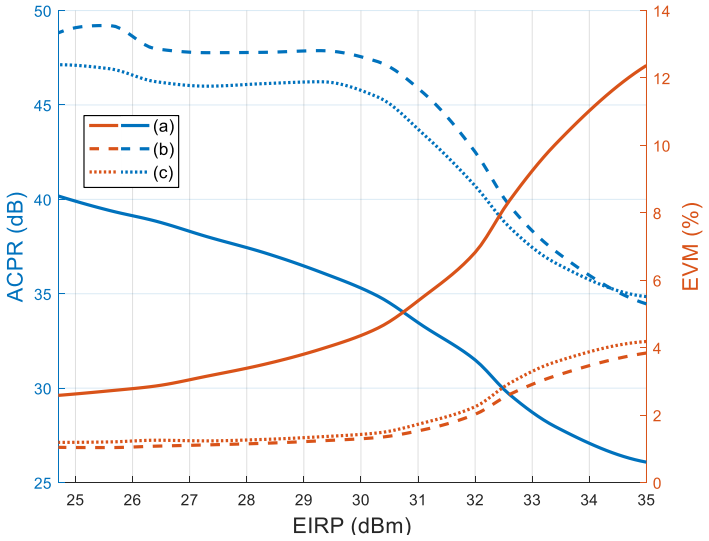

Figure 5.7: Near-field based DPD assessment: ACPR and EVM vs. EIRP (a) before DPD, (b) after DPD trained using far-field based TOR [24], (c) after DPD trained using near-field based TOR [4]

Chapter 6

Conclusions and Future Work

As commercial wireless communication progresses with the deployment of 5G, more and more attention has been paid to mm-wave bands as they provide wider channel bandwidths for increased data speeds. At these frequencies, beamforming arrays are used to increase link distance, improve the receiver signal-to-noise ratio, and to enable MIMO operation. A significant amount of research has been conducted into realizing competitive array hardware and improving signal quality.

However, the problem is that mm-wave beamforming arrays require calibration and linearization to achieve the best performance and efficiency, and these processes traditionally require extra hardware. To solve this problem, an integrated and inexpensive architecture is needed where the array and the TOR are a self-contained unity. Based on theory, the integrated TOR needs to have uniform coupling to all antenna elements, it needs linear and flat frequency responses, and it needs to be generic and applicable to planar arrays of any size. Previous works proposed a mutual coupling-based solution, where additional antenna elements are placed around the main array to gather the transmitted signals. This solution works well in small arrays but is not scalable. Other works proposed a coupler-based approach, which is scalable, but sacrifices antenna element spacing, making the array unsuitable for RF beamforming. This thesis proposes a near-field probing array architecture that meets the abovementioned requirements; the theoretical derivation and experimental validation proved that it is a viable solution for in-field array self-calibration and DPD linearization.

The main antenna array element in the RF beamforming array is designed as a coaxial fed patch antenna, implemented using modern PCB technology. In order to reduce fabrication cost and risk, the initial prototype is designed in two separated PCBs with the

same stack up. The primary PCB contains patch antenna and near-field probing arrays, while the secondary PCB houses the RFIC and RF distribution network. The two boards are assembled together using low-profile SMPM connectors. The antenna achieves 4 GHz bandwidth at 29 to 31 GHz, with around 95% radiation efficiency. The design of the embedded near-field probing array exploits the concept of parasitic elements in order to minimize the impact of the near-field probes on the array's radiation performance, and improve probe input impedance matching. The near-field probe is located at the center of each four beamforming antenna elements, so that it has the highest coupling to these four elements, at around -13 dB, and low coupling magnitude to the other elements at below -20 dB. The array is designed based on this modular four-element unit cell, so the array size is not limited. The probe is input matched at 29 GHz and has a flat mutual coupling magnitude from 27 to 30 GHz.

A prototype 16-element array is fabricated first, which is used to validate the proposed near-field based calibration scheme. Two sets of experiments were conducted, using 1) a CW signal and 2) a 400 MHz OFDM modulated signal. At 28.75 GHz, the post-calibration array achieves phase and amplitude errors of 2.8 ° and 0.27 dB, respectively. Using DPD trained with the near-field probing array fed TOR, and various DPD schemes proposed in the literature, the ACPR and EVM improved from 30 dB and 8.8% to 39 dB and 2.5% for an EIRP of 33 dBm. Using the newly proposed method of estimating near-field channel and training DPD engine accordingly, ACPR and EVM improved from 29.66 dB to 40.49 dB, and 8.29% to 2.4%. From these experimental validations, it can be concluded that the proposed near-field probing array serves well as a feedback path for array calibration and DPD, and is a viable option that can be added to a regular RF beamforming array. The problem this thesis focuses on is successfully addressed.

The PCB manufacturing process consideration involved in designing RF beamforming array is also discussed. Modern PCB stack up is mostly built following two processes: multi-lamination and HDI; based on the analysis, the array is chosen to be manufactured on a simple symmetrical multi-lamination stack up which supports both the RFIC and the antenna. In this stack up only two mechanical vias are used, and all RF signal transition uses mechanical via instead of stacked via to achieve the best and predictable performance. Many other aspects involved in the application and designing the array and near-field probe are also covered in the discussion, including far and near-field based calibration procedures and realistic coupler choices.

The thesis also presented the second generation of the RF beamforming array which uses a more advanced PCB stack up and eliminates the short come of using RF adapters between the front-end and antennas. At the time of writing this thesis, the prototype board is in fabrication.

6.1 Future Work

In the current design, every near-field probe must be utilized to perform array calibration and DPD training. This is because the highest coupling levels are found between the four surrounding elements and the probe. In this configuration, for every N array element, N/4 probes are needed. This ratio of probes to antenna elements is acceptable for smaller arrays; however, for large arrays with thousands of elements, the number of probes would be substantial. In general, even for small arrays, the fewer probes that are required, the less time the calibration process will take and the lower the bill of the material cost will be. Therefore, future work on this subject should investigate the minimum number of near-field probes needed and their optimal distribution to meet calibration and DPD training targets.

Because the theory of the near-field probe is generic, it is possible to extend the existing 28 GHz design to a higher frequency and cover the entire FR2 range. From another perspective, mm-wave dual-polarized beamforming phased arrays start to show their advantages in doubling the link speed, power, and enabling polarization-diversity based MIMO. It would be useful to expand this work into a dual-polarized design in the future.

References

[1] 3GPP. 3GPP Release 16. Available at https://www.3gpp.org/release-16.

[2] 3GPP. 5G; NR; Base Station (BS) radio transmission and reception (3GPP TS 38.104 version 15.9.0 Release 15), Apr. 2020.

[3] Anokiwave. AWMF-0162, Accessed Jun. 06, 2021. Available at https://www.anokiwave.com/products/awmf-0162/index.html.

[4] A. B. Ayed, Y. Cao, P. Mitran, and S. Boumaiza. Digital Predistortion of Millimeter-Wave Arrays Using Near-field-Based Transmitter Observation Receivers. *IEEE Transactions on Microwave Theory and Techniques*, 2021 (under review).

[5] A. B. Ayed, G. Scarlato, P. Mitran, and S. Boumaiza. On the Effectiveness of Near-Field Feedback for Digital Pre-Distortion of Millimeter-Wave RF Beamforming Arrays. In *2020 IEEE/MTT-S International Microwave Symposium (IMS)*, pages 547–550, 2020.

[6] Chun-Nien Chen, Yi-Hsien Lin, Li-Cheng Hung, Tzu-Chien Tang, Wei-Pang Chao, Cheng-Yu Chen, Po-Hsiang Chuang, Guan-Yu Lin, Wei-Jun Liao, Yu-Hsiang Nien, Wei-Cheng Huang, Tai-Yu Kuo, Kun-You Lin, Tian-Wei Huang, Yi-Cheng Lin, Hsin-Chia Lu, Tsung-Heng Tsai, and Huei Wang. 38-GHz Phased Array Transmitter and Receiver Based on Scalable Phased Array Modules With Endfire Antenna Arrays for 5G MMW Data Links. *IEEE Transactions on Microwave Theory and Techniques*, 69(1):980–999, 2021.

[7] Ching-Yun Chu, Yuan-Pu Chen, Jing-Zhi Gao, Cheng-Yung Ke, Yu-Wei Chen, Li-Han Chang, Borching Su, Ta-Shun Chu, and Yu-Jiu Wang. A Ka-Band Scalable Hybrid Phased Array Based on Four-Element ICs. *IEEE Transactions on Microwave Theory and Techniques*, 68(1):288–300, 2020.

[8] Cisco. Cisco Visual Networking Index: Global Mobile Data Traffic Forecast Update, 2017–2022. Available at https://s3.amazonaws.com/media.mediapost.com/uploads/CiscoForecast.pdf.

[9] Xiaohu Fang, Jingjing Xia, and Slim Boumaiza. A 28-GHz Beamforming Doherty Power Amplifier With Enhanced AM-PM Characteristic. *IEEE Transactions on Microwave Theory and Techniques*, 68(7):3017–3027, 2020.

[10] Saswati Ghosh and Debarati Sen. An Inclusive Survey on Array Antenna Design for Millimeter-Wave Communications. *IEEE Access*, 7:83137–83161, 2019.

[11] Xiaoxiong Gu, Duixian Liu, Christian Baks, Ola Tageman, Bodhisatwa Sadhu, Joakim Hallin, Leonard Rexberg, Pritish Parida, Young Kwark, and Alberto Valdes-Garcia. Development, Implementation, and Characterization of a 64-Element Dual-Polarized Phased-Array Antenna Module for 28-GHz High-Speed Data Communications. *IEEE Transactions on Microwave Theory and Techniques*, 67(7):2975–2984, 2019.

[12] Xiaoxiong Gu, Duixian Liu, and Bodhisatwa Sadhu. Packaging and Antenna Integration for Silicon-Based Millimeter-Wave Phased Arrays: 5G and Beyond. *IEEE Journal of Microwaves*, 1(1):123–134, 2021.

[13] Jian-Ming Jin. *Theory and Computation of Electromagnetic Fields*. Wiley, 2010.

[14] Kerim Kibaroglu, Mustafa Sayginer, Thomas Phelps, and Gabriel M. Rebeiz. A 64-Element 28-GHz Phased-Array Transceiver With 52-dBm EIRP and 8–12-Gb/s 5G Link at 300 Meters Without Any Calibration. *IEEE Transactions on Microwave Theory and Techniques*, 66(12):5796–5811, 2018.

[15] Umut Kodak, Bhaskara Rupakula, Samet Zihir, and Gabriel M. Rebeiz. 60-GHz 64- and 256-Element Dual-Polarized Dual-Beam Wafer-Scale Phased-Array Transceivers With Reticle-to-Reticle Stitching. *IEEE Transactions on Microwave Theory and Techniques*, 68(7):2745–2767, 2020.

[16] Toshihide Kuwabara, Noriaki Tawa, Yuichi Tone, and Tomoya Kaneko. A 28 GHz 480 elements digital AAS using GaN HEMT amplifiers with 68 dBm EIRP for 5G long-range base station applications. In *2017 IEEE Compound Semiconductor Integrated Circuit Symposium (CSICS)*, pages 1–4, 2017.

[17] Marko E. Leinonen, Markku Jokinen, Nuutti Tervo, Olli Kursu, and Aarno Pärssinen. System EVM Characterization and Coverage Area Estimation of 5G Directive mmW

Links. *IEEE Transactions on Microwave Theory and Techniques*, 67(12):5282–5295, 2019.

[18] X. Liu, W. Chen, L. Chen, F. M. Ghannouchi, and Z. Feng. Linearization for Hybrid Beamforming Array Utilizing Embedded Over-the-Air Diversity Feedbacks. *IEEE Transactions on Microwave Theory and Techniques*, 67(12):5235–5248, 2019.

[19] Michael Matthews, Ken Holcomb, Jim Haley, and Catherine Shearer. PTH Core-to-Core Interconnect Using Sintered Conductive Pastes. Available at https://smtnet.com/library/files/upload/Sintered-Conductive-Pastes.pdf.

[20] Rosanah Murugesu, Michael Holyoak, Hungkei Chow, and Shahriar Shahramian. Linearization of mm-Wave Large-Scale Phased Arrays Using Near-Field Coupling Feedback for ¿10Gb/s Wireless Communication. In *2020 IEEE/MTT-S International Microwave Symposium (IMS)*, pages 1271–1274, 2020.

[21] Ahmed Nafe, Kerim Kibaroglu, Mustafa Sayginer, and Gabriel M. Rebeiz. An In-Situ Self-Test and Self-Calibration Technique Utilizing Antenna Mutual Coupling for 5G Multi-Beam TRX Phased Arrays. In *2019 IEEE MTT-S International Microwave Symposium (IMS)*, pages 1229–1232, 2019.

[22] Ahmed Nafe, Mustafa Sayginer, Kerim Kibaroglu, and Gabriel M. Rebeiz. 2×64-Element Dual-Polarized Dual-Beam Single-Aperture 28-GHz Phased Array With 2×30 Gb/s Links for 5G Polarization MIMO. *IEEE Transactions on Microwave Theory and Techniques*, 68(9):3872–3884, 2020.

[23] Muhammad Imran Nawaz, Zhao Huiling, Muhammad Sabir Sultan Nawaz, Khalid Zakim, Shah Zamin, and Aurangzeb Khan. A review on wideband microstrip patch antenna design techniques. In *2013 International Conference on Aerospace Science Engineering (ICASE)*, pages 1–8, 2013.

[24] E. Ng, Y. Beltagy, G. Scarlato, A. Ben Ayed, P. Mitran, and S. Boumaiza. Digital Predistortion of Millimeter-Wave RF Beamforming Arrays Using Low Number of Steering Angle-Dependent Coefficient Sets. *IEEE Transactions on Microwave Theory and Techniques*, 67(11):4479–4492, 2019.

[25] Nokia. 5G - ready for business, Accessed Jun. 06, 2021. Available at https://www.nokia.com/networks/5g/readiness-report/5g-ready-for-business/.

[26] Nicholas Peccarelli and Caleb Fulton. A Mutual Coupling Approach to Digital Pre-Distortion and Nonlinear Equalization Calibration for Digital Arrays. In *2019 IEEE*

International Symposium on Phased Array System Technology (PAST), pages 1–8, 2019.

[27] David M. Pozar. *Microwave Engineering*. Wiley, 2012.

[28] Qorvo. An Essential of the Wi-Fi Tri-Band System. Available at https://www.qorvo.com/design-hub/blog/wifi-5-point-2-ghz-rf-filters.

[29] Qualcomm. What is 5G. Available at https://www.qualcomm.com/5g/what-is-5g.

[30] RENESAS. IDT Wafer-level Chip Scale Package (WLCSP) Implementation Guidelines, 2016. [Online].

[31] Bhaskara Rupakula, Abdurrahman H. Aljuhani, and Gabriel M. Rebeiz. ACPR Improvement in Large Phased Arrays With Complex Modulated Waveforms. *IEEE Transactions on Microwave Theory and Techniques*, 68(3):1045–1053, 2020.

[32] Bhaskara Rupakula, Ahmed Nafe, Samet Zihir, Yaochen Wang, Tsu-Wei Lin, and Gabriel Rebeiz. 63.5–65.5-GHz Transmit/Receive Phased-Array Communication Link With 0.5–2 Gb/s at 100–800 m and ± 50° Scan Angles. *IEEE Transactions on Microwave Theory and Techniques*, 66(9):4108–4120, 2018.

[33] Bodhisatwa Sadhu, Xiaoxiong Gu, and Alberto Valdes-Garcia. The more (antennas), the merrier: A survey of silicon-based mm-wave phased arrays using multi-ic scaling. *IEEE Microwave Magazine*, 20(12):32–50, 2019.

[34] Scarlato, Giovanni. Design of 28 GHz 4x4 RF Beamforming Array for 5G Radio Front-Ends, 2019.

[35] Christian M. Schmid, Stefan Schuster, Reinhard Feger, and Andreas Stelzer. On the Effects of Calibration Errors and Mutual Coupling on the Beam Pattern of an Antenna Array. *IEEE Transactions on Antennas and Propagation*, 61(8):4063–4072, 2013.

[36] Parastoo Taghikhani, Koen Buisman, and Christian Fager. Hybrid Beamforming Transmitter Modeling for Millimeter-Wave MIMO Applications. *IEEE Transactions on Microwave Theory and Techniques*, 68(11):4740–4752, 2020.

[37] Nuutti Tervo, Bilal Khan, Olli Kursu, Janne P. Aikio, Markku Jokinen, Marko E. Leinonen, Markku Juntti, Timo Rahkonen, and Aarno Pärssinen. Digital Predistortion of Phased-Array Transmitter With Shared Feedback and Far-Field Calibration. *IEEE Transactions on Microwave Theory and Techniques*, 69(1):1000–1015, 2021.

[38] Norfishah Ab Wahab, Siti Aminah Nordin, Wan Norsyafizan W. Muhamad, and Suzi Seroja Sarnin. Microstrip Rectangular Inset-Fed Patch Array Antenna for WiMax Application. In *2020 IEEE International RF and Microwave Conference (RFM)*, pages 1–4, 2020.

[39] Yun Wang, Rui Wu, Jian Pang, Dongwon You, Ashbir Aviat Fadila, Rattanan Saengchan, Xi Fu, Daiki Matsumoto, Takeshi Nakamura, Ryo Kubozoe, Masaru Kawabuchi, Bangan Liu, Haosheng Zhang, Junjun Qiu, Hanli Liu, Naoki Oshima, Keiichi Motoi, Shinichi Hori, Kazuaki Kunihiro, Tomoya Kaneko, Atsushi Shirane, and Kenichi Okada. A 39-GHz 64-Element Phased-Array Transceiver With Built-In Phase and Amplitude Calibrations for Large-Array 5G NR in 65-nm CMOS. *IEEE Journal of Solid-State Circuits*, 55(5):1249–1269, 2020.

[40] Binqi Yang, Zhiqiang Yu, Ji Lan, Ruoqiao Zhang, Jianyi Zhou, and Wei Hong. Digital Beamforming-Based Massive MIMO Transceiver for 5G Millimeter-Wave Communications. *IEEE Transactions on Microwave Theory and Techniques*, 66(7):3403–3418, 2018.

[41] Yusheng Yin, Samet Zihir, Tumay Kanar, Qian Ma, Hyunchul Chung, Li Gao, and Gabriel M. Rebeiz. A 37–42-GHz 8 $\times$ 8 Phased-Array With 48–51-dBm EIRP, 64–QAM 30-Gb/s Data Rates, and EVM Analysis Versus Channel RMS Errors. *IEEE Transactions on Microwave Theory and Techniques*, 68(11):4753–4764, 2020.

[42] C. Yu, J. Jing, H. Shao, Z. H. Jiang, P. Yan, X. Zhu, W. Hong, and A. Zhu. Full-Angle Digital Predistortion of 5G Millimeter-Wave Massive MIMO Transmitters. *IEEE Transactions on Microwave Theory and Techniques*, 67(7):2847–2860, 2019.

[43] Samet Zihir, Ozan Dogan Gurbuz, Arjun Kar-Roy, Sanjay Raman, and Gabriel M. Rebeiz. 60-GHz 64- and 256-Elements Wafer-Scale Phased-Array Transmitters Using Full-Reticle and Subreticle Stitching Techniques. *IEEE Transactions on Microwave Theory and Techniques*, 64(12):4701–4719, 2016.